Mineral dust aerosols in the NASA Goddard Institute for Space Sciences ModelE atmospheric general circulation model

R. L. Miller,[1,2] R. V. Cakmur,[2,3] J. Perlwitz,[1,2] I. V. Geogdzhayev,[1,2] P. Ginoux,[4] D. Koch,[2,5] K. E. Kohfeld,[6] C. Prigent,[7] R. Ruedy,[2] G. A. Schmidt,[2,5] and I. Tegen[8]

Received 24 January 2005; revised 19 October 2005; accepted 17 November 2005; published 29 March 2006.

[1] We describe an updated model of the dust aerosol cycle embedded within the NASA Goddard Institute for Space Studies 'ModelE' atmospheric general circulation model (AGCM). The model dust distribution is compared to observations ranging from aerosol optical thickness and surface concentration to deposition and size distribution. The agreement with observations is improved compared to previous distributions computed by either an older version of the GISS AGCM or an offline tracer transport model. The largest improvement is in dust transport over the Atlantic due to increased emission over the Sahara. This increase comes from subgrid wind fluctuations associated with dry convective eddies driven by intense summertime heating. Representation of 'preferred sources' of soil dust particles is also fundamental to the improvement. The observations suggest that deposition is too efficient in the model, partly due to AGCM rainfall errors.

Citation: Miller, R. L., et al. (2006), Mineral dust aerosols in the NASA Goddard Institute for Space Sciences ModelE atmospheric general circulation model, *J. Geophys. Res.*, *111*, D06208, doi:10.1029/2005JD005796.

1. Introduction

[2] Variations in atmospheric composition have long been recognized as a source of climate change. Warming during the late twentieth century is attributed primarily to greenhouse gases like carbon dioxide, although in recent decades the offsetting effect of aerosols has been recognized [*Charlson et al.*, 1992; *Penner et al.*, 2001]. Changes to the concentration of carbon dioxide, the leading twentieth-century climate forcing [*Hansen and Sato*, 2001], can be detected with measurements at only a few locations, because the multi-decadal lifetime of the gas allows it to be mixed throughout the globe. In contrast, aerosols are removed from the atmosphere within days to weeks, resulting in much larger spatial variations. This means that aerosols must be sampled within a comparatively dense network as their concentration changes rapidly along their trajectory. No observing network exists for aerosols analogous to the synoptic network of radiosondes that routinely measures the three-dimensional evolution of weather.

[3] Mineral (or 'soil') dust, raised by the wind erosion of dry soil particles, makes a leading contribution to the global aerosol load [*Andreae*, 1995; *Tegen et al.*, 1997]. Despite its importance, the global distribution of dust remains uncertain, even with an increasingly dense array of observing sites [*Prospero*, 1996; *Kohfeld and Harrison*, 2001; *Holben et al.*, 2001]. Satellites provide more complete spatial coverage, but in general retrieve only column integrals of dust properties like optical thickness [*Herman et al.*, 1997; *Mishchenko et al.*, 1999; *Chu et al.*, 2002; *Kahn et al.*, 2005]. To integrate these observational constraints into an evolving three-dimensional picture, models of the dust cycle are used. Among aerosols, representation of the dust cycle is a particular challenge for global models, whose estimates of global emission vary by over a factor of two [*Zender et al.*, 2004]. This range results from the use of different subsets of the available data to constrain each model, but also from different physical representations of the dust cycle. While it is agreed that regions of sediment accumulation like the dry beds of former lakes are prolific dust sources [*Prospero et al.*, 2002], model emission is highly dependent upon the specific identification of these regions [*Cakmur et al.*, 2006]. Moreover, while the models resolve the planetary-scale winds that disseminate dust worldwide, entrance of dust into the atmosphere often occurs as a result of winds whose scales are below the model resolution [*Sinclair*, 1969; *Rennó et al.*, 1998]. Because wind erosion is parameterized rather than explicitly simulated by global models, confidence in the models' physical basis requires a thorough comparison to a wide range of observations.

[1]Department of Applied Physics and Applied Math, Columbia University, New York, New York, USA.
[2]NASA Goddard Institute for Space Studies, New York, New York, USA.
[3]National Academy of Sciences, Washington, D. C., USA.
[4]Geophysical Fluid Dynamics Laboratory, NOAA, Princeton, New Jersey, USA.
[5]Center for Climate Systems Research, Columbia University, New York, New York, USA.
[6]School of Earth and Environmental Sciences, Queens College, City University of New York, Flushing, New York, USA.
[7]Laboratoire d'Études du Rayonnement et de la Matière en Astrophysique, Observatoire de Paris, CNRS, Paris, France.
[8]Leibniz Institute for Tropospheric Research, Leipzig, Germany.

0148-0227/06/2005JD005796$09.00

[4] In this article, we describe a dust model embedded within the newly available version of the NASA Goddard Institute for Space Studies (GISS) atmospheric general circulation model (AGCM), referred to as 'ModelE' [*Schmidt et al.*, 2006]. The dust model has been substantially updated in order to reflect newly available measurements along with improved representations of the dust cycle. The dust model is described in section 2, and compared to the previous version described by *Tegen and Miller* [1998]. Model emission is chosen so that the dust cycle agrees optimally with a worldwide compilation of observations, including satellite retrievals and sun photometer measurements of aerosol optical thickness, along with measurements of surface concentration and deposition, and retrievals of aerosol size distribution. Derivation of the optimal global emission is described in a companion article [*Cakmur et al.*, 2006]. Here, we evaluate the optimal case in comparison to regional measurements (section 3), and note the sensitivity of the optimal case to new aspects of the model (section 4), using the observations to identify those changes that contribute to the largest improvement. Our conclusions are presented in section 5.

2. Model Description

[5] Our description of the dust model emphasizes those features that have been updated from the previous version [*Tegen and Miller*, 1998]. The global distribution of dust evolves with the meteorology and surface conditions computed by the ModelE AGCM. ModelE is a substantial revision to the previous generation of AGCM at NASA GISS. It is described and compared to observations of the current climate by *Schmidt et al.* [2006]. ModelE is available to the community at ⟨http://www.giss.nasa.gov/tools/modelE⟩.

[6] The AGCM has horizontal resolution of 4° latitude by 5° longitude. Tracer advection is based upon the quadratic upstream scheme [*Prather*, 1986], which calculates as prognostic variables not only the mean tracer value within a grid box, but its slope and curvature, effectively increasing the resolution of dust and other tracers above the nominal value. In ModelE, the slope and curvature are now updated by the aerosol deposition schemes, resulting in more accurate simulation of these processes [*Ginoux*, 2003]. The model top has been raised from 10 to 0.1 mb near the stratopause, and the number of vertical layers has been increased to 20, with six new layers added to the stratosphere. Two new layers increase resolution within the lower troposphere, which is significant for the surface wind that raises dust. Mixing within the planetary boundary layer (PBL) is now based upon a non-local parameterization [*Cheng et al.*, 2002, 2003, 2004]. While turbulent mixing was limited to the lowest layer in the previous model, it can now occur anywhere within the column as a result of static or shear instability. The model physics time step has been cut in half to thirty minutes, so that radiative and surface fluxes (including dust emission and deposition) are computed twice as often compared to the previous AGCM.

[7] Dust in ModelE is represented by four tracers distinguished by particle size. The clay category includes particles with radii less than 1 μm, while the three silt classes have radii between 1–2, 2–4, and 4–8 μm, respectively.

[8] The most prolific sources of dust aerosol are arid lowlands where soil particles are accumulated by fluvial erosion of the surrounding mountains [*Prospero et al.*, 2002]. The dry beds of former lakes are especially productive. In this article, these 'preferred sources' correspond to the topographic depressions identified by *Ginoux et al.* [2001]. The effect of other erodibility prescriptions [*Tegen et al.*, 2002; *Zender et al.*, 2003; *Grini et al.*, 2005] upon the dust cycle is considered in our companion study [*Cakmur et al.*, 2006]. Dust sources created by human disturbance of the soil, through agriculture, overgrazing, and deforestation, for example, are currently omitted from this model, in contrast to *Tegen and Miller* [1998], where roughly half of the emission was anthropogenic. The anthropogenic contribution to global emission is smaller according to more recent estimates, although the precise value is not settled [*Mahowald and Luo*, 2003; *Tegen et al.*, 2004a; *Mahowald et al.*, 2004; *Tegen et al.*, 2004b].

[9] Dust emission is inhibited by vegetation, which shields soil particles from the force of the wind. *Tegen and Miller* [1998] allow emission over regions of grassland, shrubland, or desert identified by *Matthews* [1983]. Here, we identify soils exposed to the wind using a more direct criterion based upon surface roughness, retrieved from measurements of a surface-reflected microwave pulse with a scatterometer on board the European Remote Sensing (ERS) satellite, and calibrated using in situ roughness measurements [*Prigent et al.*, 2005]. This data set characterizes surface roughness at roughly 50 km resolution, which is comparable to the *Matthews* [1983] vegetation data. We allow emission to occur in the fraction of the AGCM grid box where the ERS roughness parameter falls below −13 dB, corresponding to a roughness length of about 0.1 cm. This allows roughly one-quarter of the total land grid boxes to act as a potential dust source, consistent with previous studies [e.g., *Tegen and Fung*, 1994]. However, emission occurs within only a small fraction of each grid box, representing the geographic confinement of preferred sources. For the *Ginoux et al.* [2001] prescription used in this study, the total source extent is 0.69% of the global surface area [*Cakmur et al.*, 2006]. We update the ERS value each month to represent the seasonal cycle of vegetation. The effect of roughness as opposed to vegetation as a criterion for emission is compared in section 4.

[10] According to wind tunnel measurements, soil particles enter the atmosphere when the wind stress exceeds a certain threshold [e.g., *Gillette*, 1974]. This initiates saltation, a horizontal creep of particles with radius of order 30 μm and larger [*Marticorena and Bergametti*, 1995]. The collision of saltating particles with the surface can liberate the smaller particles that are dispersed globally and have the greatest radiative effect [*Shao et al.*, 1993; *Shao*, 2001]. Representation of the latter process (called 'sandblasting') requires detailed knowledge of the saltator size distribution, which is related to the size distribution of soil particles at each location [*Alfaro and Gomes*, 2001; *Grini et al.*, 2002]. Sandblasting also depends upon the binding energy that must be overcome to liberate the smaller particles that are potential aerosols,

which depends upon the local mineralogy. Rather than simulate this complicated process, which depends upon information that is not available for every source region worldwide, we simply assume that aerosol particles are created when the wind stress exceeds a certain threshold. In general, wind stress is related to the surface wind speed through the roughness length. We assume that dry lake beds and other environments making the greatest contribution to dust emission are similar worldwide and can be characterized by a single surface roughness. Then, emission can be expressed in terms of surface wind speed above a threshold that is globally uniform.

[11] To account for the binding effect of interstitial water upon the soil grains that are potential aerosols [*Fecan et al.*, 1999], we increase the emission threshold with soil moisture. Emission is observed to resume shortly after precipitation as long as the uppermost centimeter or so has dried out [*Gillette*, 1999]. Measurements of the relation between emission and soil moisture are difficult to apply to ModelE, where moisture is assumed to be uniform over the uppermost soil layer of 10 cm depth. Following *Shao et al.* [1996], we increase the emission threshold w_T according to the soil wetness q, defined as the water within the uppermost soil layer divided by the field capacity or maximum soil water:

$$w_T = w_{T,0} \exp[0.7q], \tag{1}$$

where $w_{T,0}$ is the emission threshold of the 10 m surface wind speed for completely dry soil (equal to 8 ms^{-1}). Saturation of the soil (corresponding to q equal to unity) increases the emission threshold by a factor of two, but even in the absence of precipitation, soil moisture remains above zero, asymptoting to a value that depends upon the soil texture. Our threshold sensitivity to soil moisture is comparable to that of *Fecan et al.* [1999], which is calibrated using wind tunnel measurements. The dependence of our results upon the threshold sensitivity is considered in section 4. Emission is prohibited entirely where the surface is covered with ice or more than 1 cm of snow.

[12] That emission is observed to occur on the scale of tens of meters to tens of kilometers [*Idso et al.*, 1972; *Sinclair*, 1973] is a challenge to global dust models, where the calculated surface wind represents an areal average over each grid box, whose horizontal extent typically exceeds a hundred kilometers. To represent wind fluctuations on smaller scales over which emission is observed to occur, we assume a probability distribution $p(w)\, dw$ of surface wind speed w within each grid box [*Cakmur et al.*, 2004]. The emission $\mathcal{E}$ is calculated according to:

$$\mathcal{E} = CF(r) \int_{w_T}^{\infty} w^2 (w - w_T) p(w)\, dw, \tag{2}$$

where C represents the efficiency of emission for a given wind event, and $F(r)$ is the fractional size distribution of the emitted particles of radius r. This distribution should strictly appear inside the integral, as it depends upon the size distribution of the saltating particles, which is a function of the surface wind speed [*Iversen and White*, 1982]. We currently neglect this dependence for simplicity, and derive a globally uniform fractional size distribution as described below.

[13] The cubic dependence of emission upon surface wind speed above a threshold in (2) is suggested by wind tunnel measurements [*Gillette*, 1974]. The probability distribution $p(w)\, dw$ constructed by *Cakmur et al.* [2004] resembles the Weibull distribution fitted empirically to wind observations [*Justus and Mikhail*, 1976; *Pavia and O'Brien*, 1986], and proposed for the calculation of dust emission [*Gillette and Passi*, 1988; *Grini and Zender*, 2004]. The distribution parameters are derived from the magnitude of subgrid wind variations calculated by the AGCM parameterizations of the PBL, along with dry and moist convection [*Cakmur et al.*, 2004]. Subgrid wind variations are dominated by the occurrence of dry convection, and increase emission preferentially over summertime deserts where intense solar heating of the surface drives vigorous mixing within the PBL. Topography and variations in surface roughness are an additional and potentially important source of subgrid wind fluctuations (through vortex shedding, for example, or channeling of the flow upwind of the Bodele Depression), although these effects are precluded by the resolution of the model.

[14] Our use of a probability distribution to represent subgrid wind variability is different from the approach of *Tegen and Miller* [1998], who introduce geographic variations in the wind speed threshold so that AGCM emission matches the value calculated by an offline model using substantially higher resolution $\left(1\frac{1}{8}^\circ \times 1\frac{1}{8}^\circ\right)$ reanalyzed winds. Lower values of the threshold are applied where the reanalyses indicate large wind variability below the scale of the AGCM grid box. Among the drawbacks of this adjustment is that it compensates for errors in the reanalysis winds, which are often based upon few actual observations in the sparsely populated arid regions that produce dust. In addition, the implied subgrid variability is constant in time rather than being correlated with frontal passage or the occurrence of dry convection, for example. In the present study, we let the AGCM identify the occurrence of large subgrid wind fluctuations based upon its calculated meteorology [*Cakmur et al.*, 2004]. This approach, where the AGCM identifies meteorology that favors or 'prefers' emission, is complementary to the enhancement of emission by preferred sources.

[15] Dust is removed from the atmosphere by a combination of wet and dry deposition. Removal by wet deposition is proportional to column precipitation, and occurs at all levels beneath the computed cloud top. In contrast, *Tegen and Miller* [1998] removed dust up to the climatological tropopause, which allowed aerosols to accumulate above this level after their introduction by penetrating convection. Modification of the removal depth has a negligible effect upon the global dust load, but reduces transport to high latitudes above the mid-latitude tropopause. Dry deposition is based upon a 'resistance in series' scheme that represents a combination of gravitational and turbulent settling [*Wesely and Hicks*, 1977; *Koch et al.*, 1999]. The Stokes speed of gravitational settling is slightly lower compared to that of *Tegen and Miller* [1998], resulting from a correction to the particle radius. In addition, the turbulent fall speed is no longer a constant but is now coupled to the magnitude of turbulence computed by the PBL parameterization [*Koch et al.*, 2006]. Dust is removed from the atmosphere at a greater rate within an actively mixed boundary layer. Both

mechanisms of dry deposition are calculated using the same scheme as other aerosols within ModelE.

[16] In the present study, dust radiative forcing is computed as a diagnostic for comparison to observations, but this forcing is omitted from the calculation of the model climate. This eliminates a feedback, because the observed dust cycle depends upon the climate, which is perturbed by dust. Disabling this feedback simplifies the derivation of the dust distribution that is in best agreement with the observations, as described below. This feedback reduces global emission by roughly 15% in a previous version of the model [*Perlwitz et al.*, 2001; *Miller et al.*, 2004a], although certain regions exhibit a slight increase [*Miller et al.*, 2004b]. The reduction exhibited by the present model is similar, as will be described separately. In either case, this feedback upon emission is small compared to the emission uncertainty, and we neglect it for convenience.

[17] To diagnose radiative forcing, dust particles are treated as Mie scatterers, where they are idealized as spheres. This idealization is justified by the good quantitative agreement between fluxes computed using nonspherical aerosols and surface or volume-equivalent spheres [*Mishchenko et al.*, 1995]. While particles with radii smaller than 1 μm are transported as a single category, due to their nearly uniform rate of gravitational settling, they are divided into four size categories for the radiative calculation, using the mass partitioning calculated explicitly by *Tegen and Lacis* [1996]. Dust radiative forcing is computed as described by *Miller et al.* [2004c], with two exceptions. First, the imaginary part of the index of refraction, formerly taken from laboratory measurements of Saharan dust collected over the Atlantic [*Patterson et al.*, 1977], is reduced by roughly two-thirds at solar wavelengths to be consistent with the value determined by *Sinyuk et al.* [2003] based upon Total Ozone Mapping Spectrometer (TOMS) retrievals and in situ sun photometer measurements from the Aerosol Robotic Network (AERONET). Outside of visible wavelengths, the imaginary index is interpolated to join smoothly with the long-wave values beyond 2 μm as measured by *Volz* [1973]. Second, scattering at thermal wavelengths, although not explicitly computed, is represented by a 30% increase in optical thickness, as suggested by the calculations of *Dufresne et al.* [2002]. This has no effect upon the optimal value of emission calculated by *Cakmur et al.* [2006], and used to calibrate global emission here (described below), because aerosol optical thickness (AOT) is a constraint only at solar wavelengths. Despite our idealization of a globally uniform index of refraction, regional variations in aerosol mineralogy and scattering are observed [*Carlson and Prospero*, 1972; *Sokolik et al.*, 1993], which introduces an error into our dust cycle that is difficult to quantify.

[18] With the exception of the control simulation, we calculate a five-year model climatology for each experiment described in the following sections, with sea surface temperature (SST) prescribed using values observed between 1997 and 2001. This period overlaps with many of the dust measurements used to evaluate the model, although the less than complete overlap introduces an uncertainty into our comparison. For the control (or 'baseline') experiment, we begin the model integration in 1992 and simulate a total of ten years. In this case, a climatology is calculated by computing the average from all possible five-year combinations within the ten-year record. This allows us to calculate the standard deviation of the five-year averages, which measures the contribution of interannual variations of SST along with the finite averaging period to the uncertainty of the climatology, as described in section 4. The standard deviation is small compared to the mean, suggesting that a five year average is sufficient to characterize the model's dust cycle.

[19] What remains to be specified in (2) are the emission efficiency C and $F(r)$, the fractional size distribution of the emitted particles. While C can be derived from wind tunnel measurements or field experiments, its value on the scale of an AGCM grid box is unclear. *Tegen and Miller* [1998] chose it to match observations of surface concentration, while the size distribution of the soil was taken from the global survey of soil texture by *Zobler* [1986]. This survey was intended for agricultural purposes and may not be appropriate for the environments that emit dust. Moreover, the emitted size distribution depends upon the redistribution of momentum from the saltating soil particles directly mobilized by the wind to the smaller particles that become aerosols [*Alfaro and Gomes*, 2001; *Grini et al.*, 2002]. Given this uncertainty, we instead derive globally uniform values of the product $CF(r)$ for clay and silt, respectively, in order to maximize the agreement of the model's climatological dust cycle with the data sets described below. (Emission by each individual silt size category is assumed to be identical.) This optimization is carried out for each experiment, allowing each version of the model to be presented in maximum agreement with the observations. Agreement is measured using the root mean square of the difference between the model and each data set. This represents the model error, which is normalized so that values of order unity represent minimal agreement with the observations, as described more fully (as the 'relevant' case) in the companion article [*Cakmur et al.*, 2006]. Because the feedback between dust radiative forcing and emission is disabled, the model dust cycle is linear with respect to the parameters C and $F(r)$. Although the absence of feedbacks slightly distorts the regional distribution of dust, this linearity allows the optimal distribution to be identified with a single integration of the model.

[20] The observations consist of seven data sets. Aerosol optical thickness is retrieved from the Advanced Very High Resolution Radiometer (AVHRR) and TOMS [*Mishchenko et al.*, 1999; *Torres et al.*, 2002], along with sun photometers from AERONET [*Holben et al.*, 2001]. While the satellite retrievals do not distinguish dust from other aerosol types, we have chosen locations for comparison where dust dominates the aerosol load. Because AOT is not retrieved in cloudy scenes, the observations are compared to clear-sky model values. Measurements of surface concentration are provided by the University of Miami network [*Prospero*, 1996]. Deposition is compiled from literature values [*Ginoux et al.*, 2001], along with values measured using marine sediment traps and compiled by DIRTMAP (Dust Indicators and Records of Terrestrial and Marine Palaeoenvironments [*Kohfeld and Harrison*, 2001; *Tegen et al.*, 2002]). Most DIRTMAP values are based upon several seasons of measurements, although a few have records as

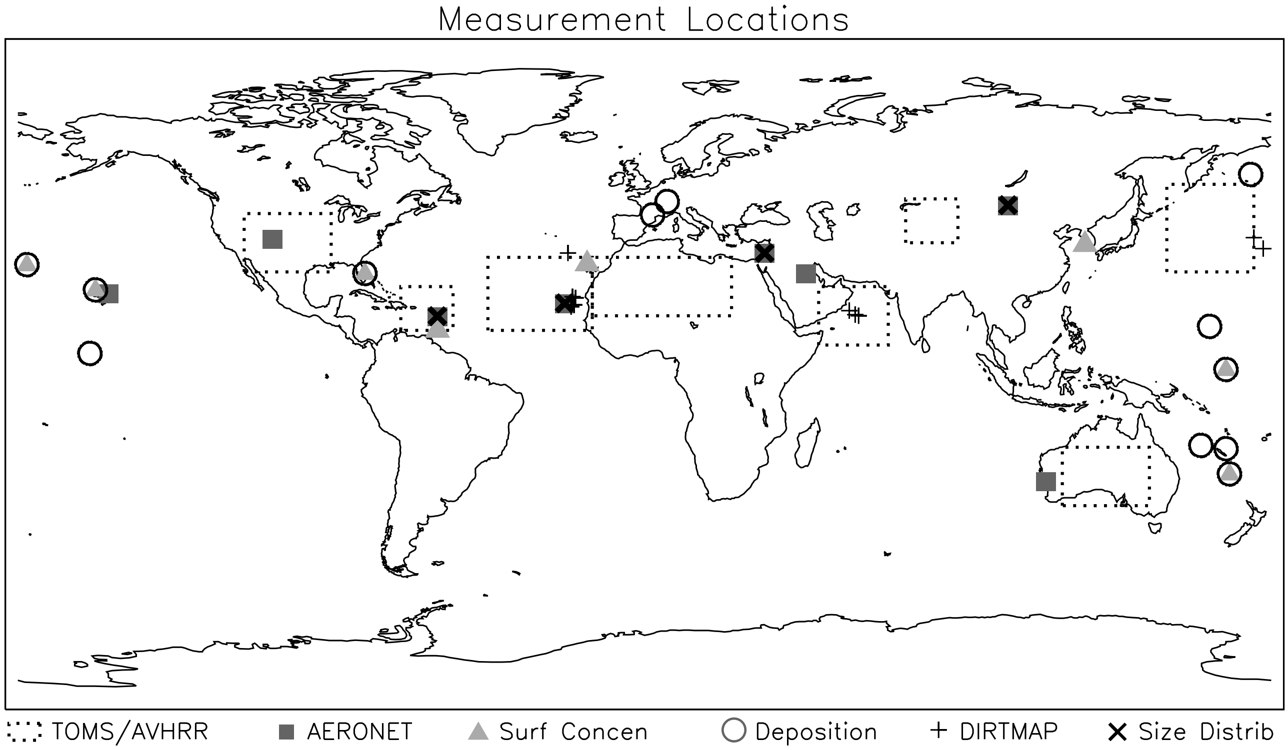

Figure 1. Locations of measurements used to evaluate the model. Satellite retrievals are averaged over the dotted regions. Squares and crosses indicate AERONET retrievals of AOT and size distribution, respectively. Triangles mark measurements of surface concentration by the University of Miami. Circles and pluses indicate measurements of deposition compiled by *Ginoux et al.* [2001] and DIRTMAP, respectively.

short as 50 days. Finally, AERONET provides retrievals of aerosol size distribution. The dust contribution is distinguished from that of other aerosol species by including only days when the total AOT exceeds 0.5, which may result in a bias when compared to the monthly mean size distributions generated by the model. These data sets and their limitations for evaluating the model dust distribution are described in greater detail in the companion article [*Cakmur et al.*, 2006].

[21] The stations used to calculate the optimal distribution for each experiment are weighted so that each major source region has nearly equal influence upon the total model error. Moreover, stations are included only if their climatology can be estimated reliably, based upon at least five years of observations (with the exception of DIRTMAP deposition measurements). Figure 1 shows the geographic distribution of stations used to assess the model in the following sections. The subset of stations used in the optimization are listed in Table 2 (as the 'relevant' case) in *Cakmur et al.* [2006].

[22] In section 4, the dust distribution from the baseline experiment is compared to a distribution calculated by the Global Aerosol Climatology Project (GACP [*Tegen et al.*, 1997]), available at ⟨www.giss.nasa.gov/data/dust⟩. The GACP distribution is included as an option in the ModelE AGCM for experiments where dust radiative forcing is needed without the computational expense of calculating a dust distribution [e.g., *Hansen et al.*, 2002]. The GACP distribution is derived from an offline tracer model driven by European Center for Medium Range Weather Forecasting reanalyzed winds, with physics similar to the AGCM version of *Tegen and Miller* [1998]. It compared well to a wide range of measurements available at the time, although it did not have the advantage of more recent data sets such as AERONET, TOMS, and the DIRTMAP compilation used here. The distribution also preceded recent improvements to dust models resulting from representations of preferred sources and subgrid wind fluctuations. The GACP distribution corresponds to global, annual emission of 1200 Tg, comprised of equal contributions from natural and anthropogenic sources. The global, annual average load is 20.2 Tg, consisting of 8.9 Tg and 11.3 Tg of clay and silt, respectively.

3. Optimal Baseline Distribution

[23] We present the global and regional distribution of dust calculated by the baseline model described in the previous section that agrees optimally with a worldwide array of measurements. This distribution is nearly identical to that derived by *Cakmur et al.* [2006] for the 'relevant' subset of observations using the *Ginoux et al.* [2001] preferred source. The only difference is that the *Cakmur et al.* [2006] distribution is formed from a single five-year climatology, whereas the baseline distribution represents the average of all five-year climatologies formed from ten years of model output (equivalent to a 10-year average). A distribution from a similar model has been submitted to

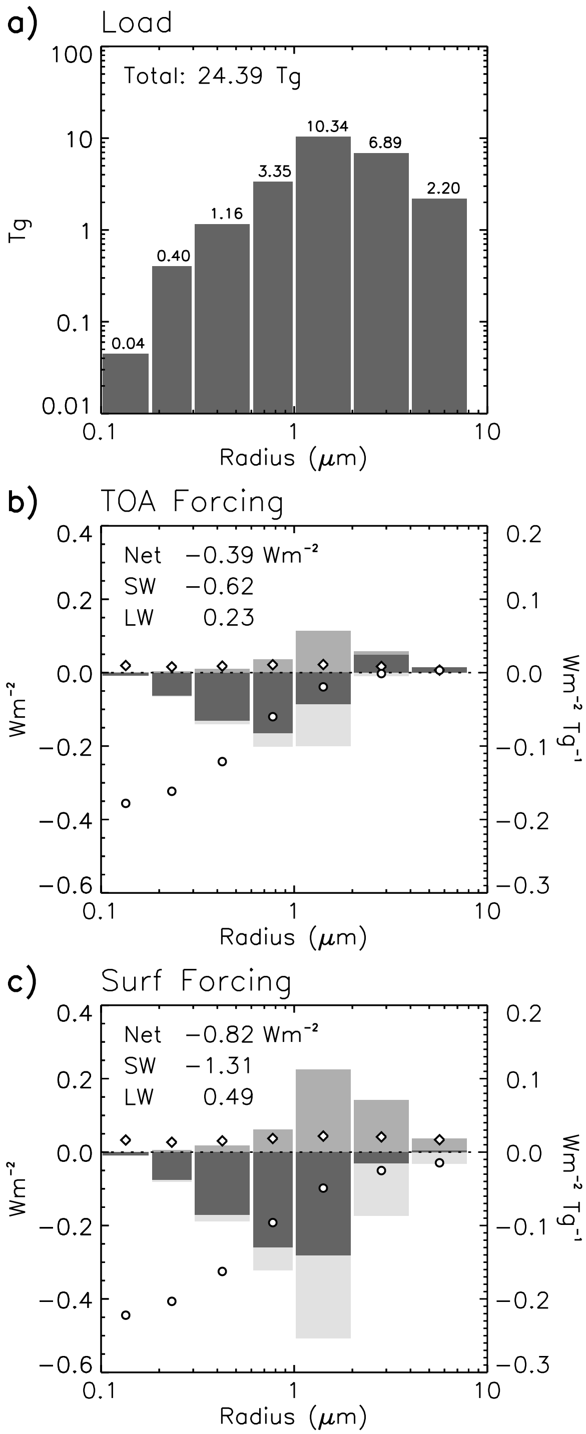

Figure 2. Global and annual average (a) dust load (Tg), and radiative forcing by dust (W m^{-2}) at the (b) top of atmosphere, and (c) surface, as a function of particle size. For radiative forcing, the shortwave, longwave, and total values correspond respectively to the light, intermediate, and dark shading. Circles and diamonds respectively denote shortwave and longwave forcing per unit mass for each size category.

AEROCOM for comparison to a different suite of observations [*Textor et al.*, 2005].

[24] Global emission for the baseline model is 1578 Tg per year, comprised of 189 Tg of clay and 1390 Tg of silt (with each silt size category contributing equally). We note that dust distributions calculated using other representations of preferred sources [*Tegen et al.*, 2002; *Zender et al.*, 2003; *Grini et al.*, 2005] agree almost equally well with the observations, but with global and annual emission as large as 2600 Tg [cf. *Cakmur et al.*, 2006, Figure 10]. The global, annual average load is 24.4 Tg. Silt particles contribute 80% of the total, with the largest contribution from particles with radii between 1 and 2 μm (Figure 2a). Our baseline case contains a substantially greater proportion of silt to clay than indicated by our previous model or other recent dust models listed in Table 1 of *Miller et al.* [2004c]. The small clay fraction minimizes the absolute model error with respect to the observations, although a clay fraction as large as two-fifths of the total load minimizes the fractional model error (the 'relevant' versus 'equal' optimization criteria in *Cakmur et al.* [2006]).

[25] The particle lifetime, which indicates the efficiency of each removal process, is listed in Table 1. The largest particles are removed primarily by gravitational settling, while wet deposition removes the smaller particles. Compared to these processes, turbulent deposition is inefficient. The wet deposition lifetime is 12.8 days, which is coincidentally identical to the value reported by *Miller et al.* [2004c] based upon the model described by *Tegen and Miller* [1998]. In contrast, dry deposition is less efficient in the current model, with a lifetime of 10.1 days compared to the previous value of 8.9 days. The total lifetime, which reflects the particle size distribution in addition to the deposition efficiency, is 5.6 days: an increase over the previous value of 5.2 days. This increase, in spite of the greater fraction of short-lived silt aerosol, results from less efficient dry removal.

[26] The global and annual average radiative forcing by dust is -0.39 Wm^{-2} at the top of the atmosphere (TOA), and -0.82 Wm^{-2} at the surface, corresponding to atmospheric heating of 0.43 Wm^{-2}. The contribution of each size category to the forcing is given by Figures 2b and 2c. Forcing is dominated by the shortwave component, with the largest contribution per unit mass by clay particles. The bulk single scatter albedo ϖ_0 (equal to the ratio of the column scattering extinction to the column total extinction) is shown for solar wavelengths in Figure 3. Around 0.5 μm where solar irradiance is largest, clay particles scatter more efficiently, while silt particles are more absorbing (Figure 3a). Increasing ϖ_0 with distance from the dust source indicates reduced absorption, as larger particles fall out preferentially along the dust plume (Figure 3b). In the solar band between 0.3 and 0.77 μm, the global and annual mean ϖ_0 is 0.955, compared to 0.906 in the previous model [*Miller et al.*, 2004c], indicating that scattering has increased at the expense of absorption. This is despite the greater fractional silt load, which replaces shortwave reflection with greater absorption at both solar and thermal wavelengths. The greater reflectivity in the present model results from our reduction of the imaginary part of the index of refraction that we prescribe for dust particles at solar wavelengths, motivated

Table 1. Lifetime (in Days) for Each Size Category[a]

	Size				
	Clay	Silt			
	0.1–1.0 μm	1–2 μm	2–4 μm	4–8 μm	All
	Dry Deposition				
Grav.	704.0	69.1	14.7	2.2	15.2
Turb.	39.7	35.4	27.5	15.1	30.0
Total	37.6	23.4	9.6	2.0	10.1
	Wet Deposition				
	12.9	12.5	12.5	15.4	12.8
	Total Deposition				
	9.6	8.1	5.4	1.7	5.6

[a]Size refers to particle radius.

by a combination of in situ measurements, satellite retrievals, and modeling [*Kaufman et al.*, 2001; *Dubovik et al.*, 2002; *Colarco et al.*, 2002; *Sinyuk et al.*, 2003].

[27] The global annual-average of clear-sky dust optical thickness is 0.0279 (with a nearly identical all-sky value). The geographic distribution is shown in Figure 4. A dust plume extends downwind from the Sahara and Sahel throughout the year. Asian sources are most active during the Northern Hemisphere (NH) spring, when severe dust storms are most frequently observed [*Zhou and Zhang*, 2003]. In addition, the plume extends to North America throughout the summer when the arrival of Asian dust is also observed [*VanCuren and Cahill*, 2002]. Compared to the previous model, the Australian source is less productive. This change results from our adoption of the topographic criterion for preferred sources [*Ginoux et al.*, 2001]. The use of other preferred source prescriptions results in larger emission from Australia [*Cakmur et al.*, 2006]. We note that there are relatively few observations within our data sets that might constrain Australian emission. The observations available in this region generally exist only for a short period of time, with a correspondingly uncertain climatology.

[28] We organize the comparison of the model dust distribution to observations of AOT (Figures 5 and 6), surface concentration (Figure 7), AERONET retrievals of size distribution (Figure 8), and deposition (Figure 9) according to the dust source, including regions downwind. The comparison is made at the stations used by *Cakmur et al.* [2006] in the 'relevant' case to optimize the distribution magnitude. We include additional stations to allow a more extensive comparison, although their climatology is uncertain due to a short observing record (and were thus excluded by *Cakmur et al.* [2006]). For the TOMS and AVHRR regional averages, the comparison is augmented by retrievals over the North Pacific, Taklimakan, North America and Australia. Rottnest Island (near Australia) is included in the AERONET AOT comparison. Nauru and Norfolk Island are added to the surface concentration comparison, while only Oahu and Midway are included in the original optimization with respect to the *Ginoux et al.* [2001] deposition data.

[29] Over the Sahara, dust AOT peaks early during NH summer (Figure 5e). While summer AOT is reproduced almost perfectly by the model, the winter value is too small by half. Similar agreement is found downwind over the eastern subtropical Atlantic (Figure 5a), Capo Verde (Figure 6b), and Izaña (Figure 7c). At the latter site, model concentration at 2500 m is plotted to correspond to the elevation of the observing station. This is near the altitude where the observed concentration within the summertime dust plume is highest [*Karyampudi and Carlson*, 1988]. The mid-summer maximum is absent in model concentration at sea level (dotted line, Figure 7c), indicating that the model plume is elevated during this

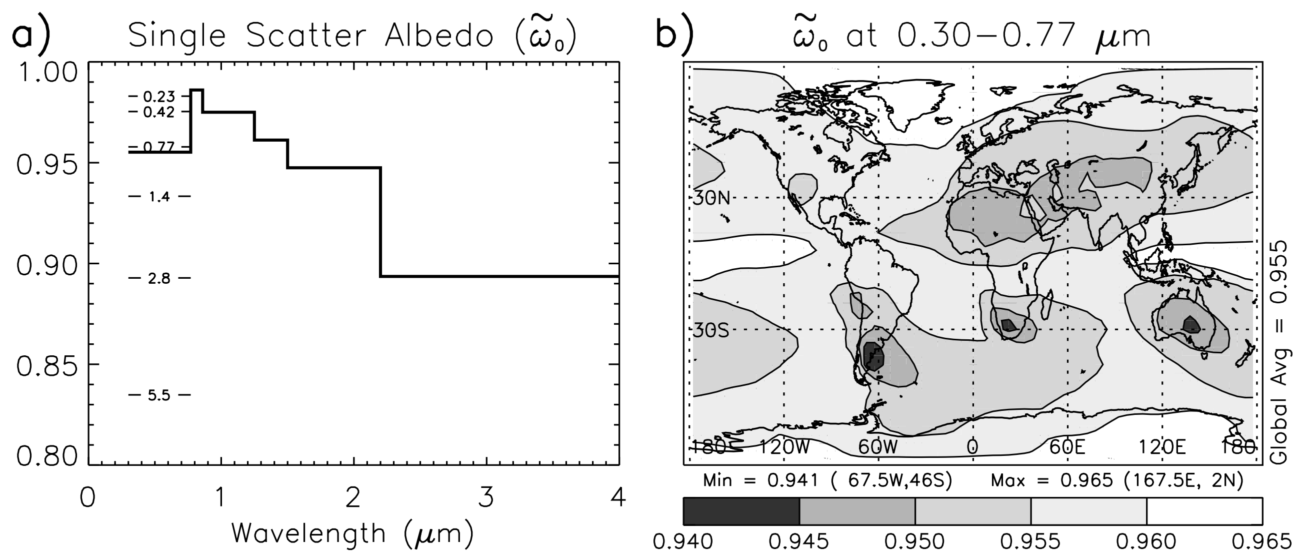

Figure 3. (a) Annual and global average of the bulk single scatter albedo ϖ_0, for the six spectral bands used in the calculation of solar radiative fluxes. The single scatter albedo is computed for each month as the ratio of the column scattering extinction and the column total extinction by dust. Also shown for the shortest solar band (0.30–0.77 μm) is the single scatter albedo for each individual particle size category, labeled by its effective radius. (b) Geographic distribution of the annual average bulk single scatter albedo at 0.3–0.77 μm.

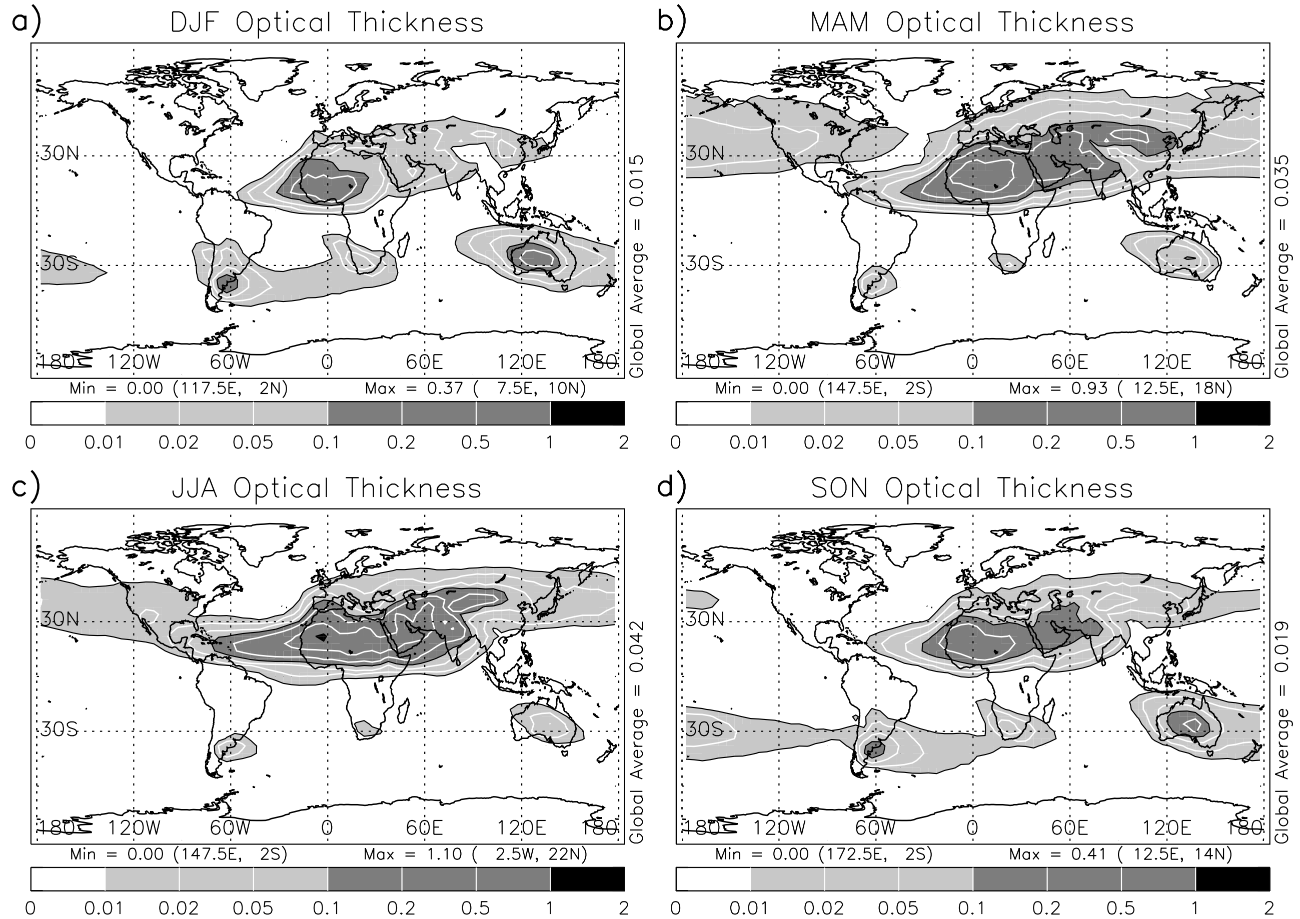

Figure 4. Clear-sky dust optical thickness for (a) DJF, (b) MAM, (c) JJA, and (d) SON.

season as observed. Farther downwind over the Caribbean, model AOT peaks a month later than indicated by AVHRR retrievals (Figure 5b) and AERONET measurements (Figure 6a), consistent with the lag in surface concentration at Barbados (Figure 7a). These figures also show that the model transports hardly any dust over the Caribbean during NH winter months. Annually-averaged measurements of deposition downwind of Saharan sources (Figure 9) indicate a slight overestimate near the source and underestimate downwind. In addition, the model overestimates the amount of silt removed between Capo Verde and Barbados during each season (Figure 8). Taken together, these errors suggest that the model overestimates removal of dust along its trajectory, due to unrealistically efficient removal or tropical precipitation that is too extensive. *Koch et al.* [2006] show that ModelE precipitation is excessive over the Caribbean throughout the year, compared to values from the Global Precipitation Climatology Project (GPCP [*Xie and Arkin*, 1997]).

[30] Downwind of the Chinese deserts, the agreement of the model with observations is contradictory. Model AOT is too small over the Taklimakan, and peaks late compared to the springtime maximum indicated by TOMS (Figure 5f). However, the agreement is substantially better downwind with respect to AERONET measurements at Dalanzadgad, where dust from the Gobi desert makes a contribution (Figures 6c and 8). At Cheju Island, south of the Korean peninsula, the model simulates the observed springtime arrival of dust, but underestimates the measured surface concentration (Figure 7b). This may result from excessive model rainfall to the west during this season [*Koch et al.*, 2006], as indicated by the GPCP. Farther downwind, at the Midway and Hawaiian Islands, the model surface concentration is in generally good agreement (Figures 7e and 7f), as is model deposition (Figure 9a). In contrast, the model underestimates AOT retrieved by AVHRR over the North Pacific (Figure 5d) and by AERONET over Mauna Loa, Hawaii (Figure 6d). The underestimate of AOT over the Pacific and far from the source, despite correct values of surface concentration and deposition, could indicate that wet deposition, which preferentially removes clay particles (whose optical extinction is large compared to silt), is excessive along the plume trajectory. This could be resolved by AERONET retrievals of the size distribution over the Pacific. Alternatively, other aerosols such as sea salt and anthropogenic sulfate could contribute to the observed AOT [*Seinfeld et al.*, 2004].

[31] Over Arabia, the model AOT is generally in agreement (Figures 6e and 6g), although retrievals of the size distribution indicate that the model silt load is too large during NH spring and summer (Figure 8), despite reasonable levels of clay. Downwind over the Arabian Sea (Figure 5c), the apparent agreement is ambiguous due to the presence of anthropogenic aerosol species [*Ramanathan et al.*, 2001].

[32] The Australian source is much less prominent compared to the previous version of our model. Over the

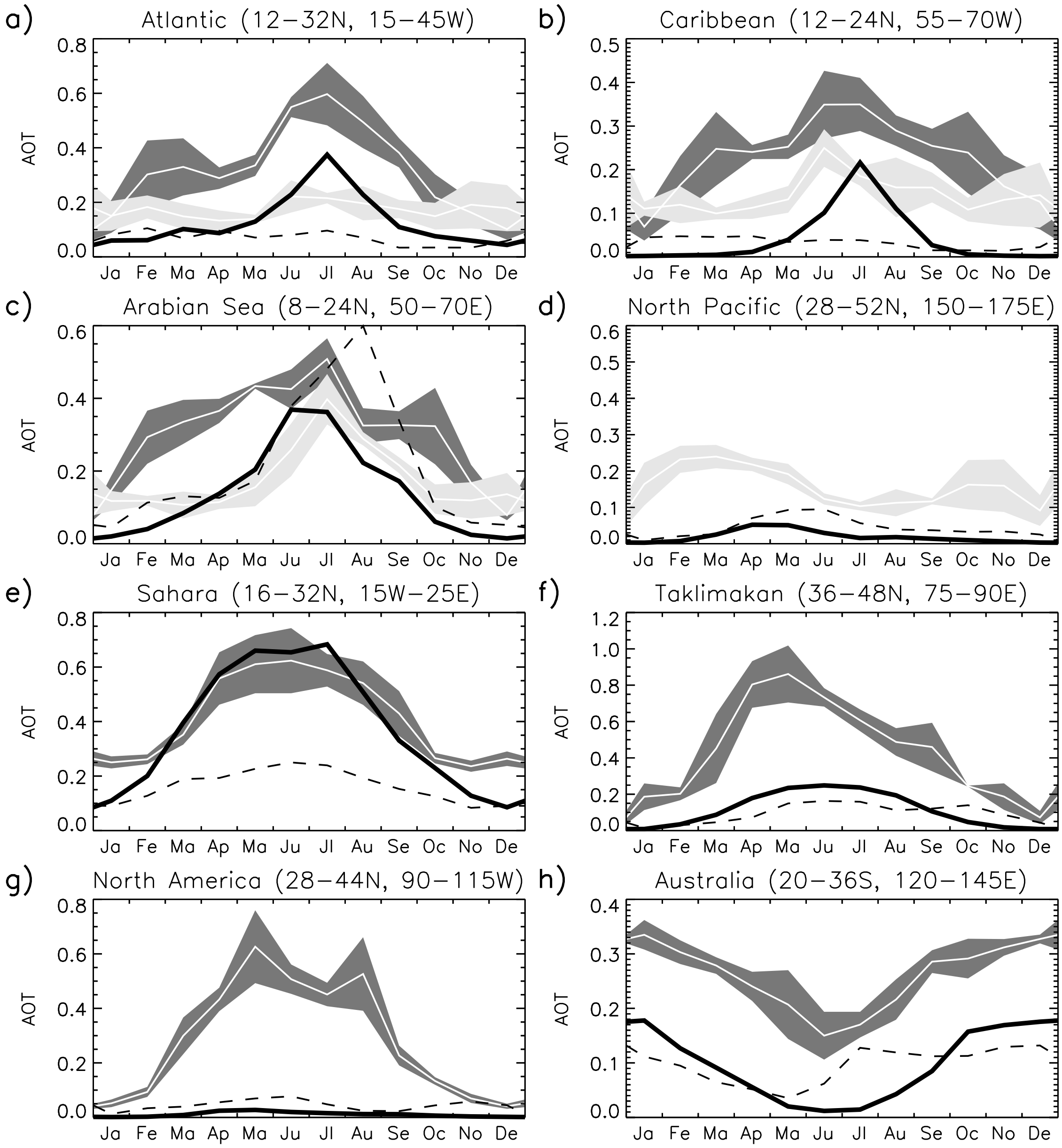

Figure 5. Comparison of clear-sky aerosol optical thickness in the baseline experiment (solid black) to TOMS and AVHRR (white) over regions where the aerosol load is dominated by dust. Shading represents interannual variability for TOMS (dark) and AVHRR (light). The dashed line shows the GACP value.

continent (Figure 5h) and downwind at Rottnest Island (Figure 6h), the annual-average model AOT is only one-third of the retrieved value, although the continental peak during Southern Hemisphere summer is reproduced. Surface concentration to the west at Norfolk is in slightly better agreement (Figure 7h). Emission in this region is sensitive to the imposed winds [*Luo et al.*, 2003], and increases in our model with the use of other representations of preferred sources [*Cakmur et al.*, 2006]. We note that this region contributes no observations to constrain the global dust load (in the 'relevant' optimization of *Cakmur et al.* [2006]), so agreement is not expected to be good. Observations of dust storm frequency could be useful to fill this gap [*Engelstaedter et al.*, 2003].

[33] Over North America, indigenous sources combine with dust transported from Asia [*VanCuren and Cahill*, 2002]. AOT retrieved by TOMS (Figure 5g) and AERONET (Figure 6f) is larger than the model AOT throughout the year. Part of the discrepancy may result from biomass burning in Central America [*Cakmur et al.*, 2004], or nearby urban sources of pollution. The agreement is improved when the model is compared to observations that distinguish dust from other aerosol types. Figure 10 shows the surface concentration of fine soil aerosol (with radii less than 1.25 μm), inferred from measurements of elemental composition by the Interagency Monitoring of Protected Visual Environments (IMPROVE) network [*Malm et al.*, 1994], averaged over two regions using the locations listed in Table 2. Over the desert and mountainous regions of western North America where emission occurs (120–105°W, 28–44°N), the model slightly overestimates the annual average, although the concentration peaks too early in the year.

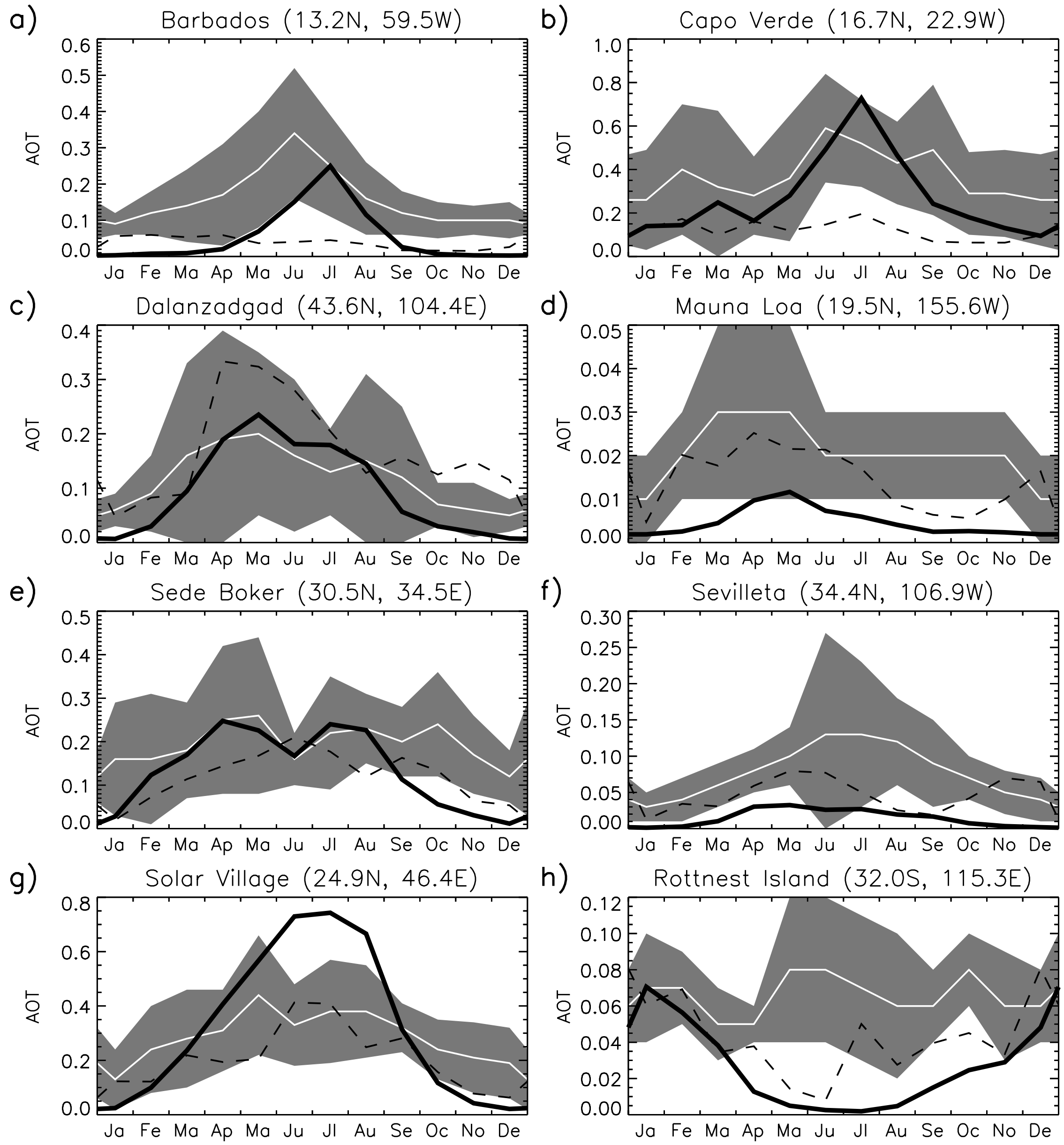

Figure 6. As in Figure 5, but for AERONET aerosol optical thickness.

Comparison of an areal average is complicated by aerosol variations associated with the complex topography that is not represented by the coarse resolution of the AGCM. In contrast, the seasonal cycle is in better agreement over the midwestern plains (105–100°W, 28–44°N), downwind from the source regions. Agreement with IMPROVE measurements occurs even though emission was not optimized using this data.

[34] In summary, the model's westward transport of Saharan dust over the Atlantic during NH summer is in good agreement with observations, although excessive deposition is indicated, and the wintertime source is too small. The Asian plume is generally realistic, although springtime emission from the Taklimakan is underestimated. The contribution of urban pollution to AOT should be included for a more definitive evaluation of transport downwind of Asian sources. Over Australia, the model AOT is comparatively small, although estimation is made difficult by the lack of observations [*Cakmur et al.*, 2006]. Observations of dust storm frequency in this region, which exist for several decades [*Engelstaedter et al.*, 2003], may reduce this uncertainty. Agreement over North America is improved by using measurements that distinguish dust from other aerosol sources.

4. Sensitivity to Model Physics

[35] Our baseline model is the result of a number of assumptions and parameter choices for which observations provide limited guidance. In this section, we consider the sensitivity of the model behavior. We also compare the quality of the simulation to previous model versions to consider whether the comparatively elaborate physics of the baseline model represents any progress in fidelity. The alternate model versions are summarized in Table 3.

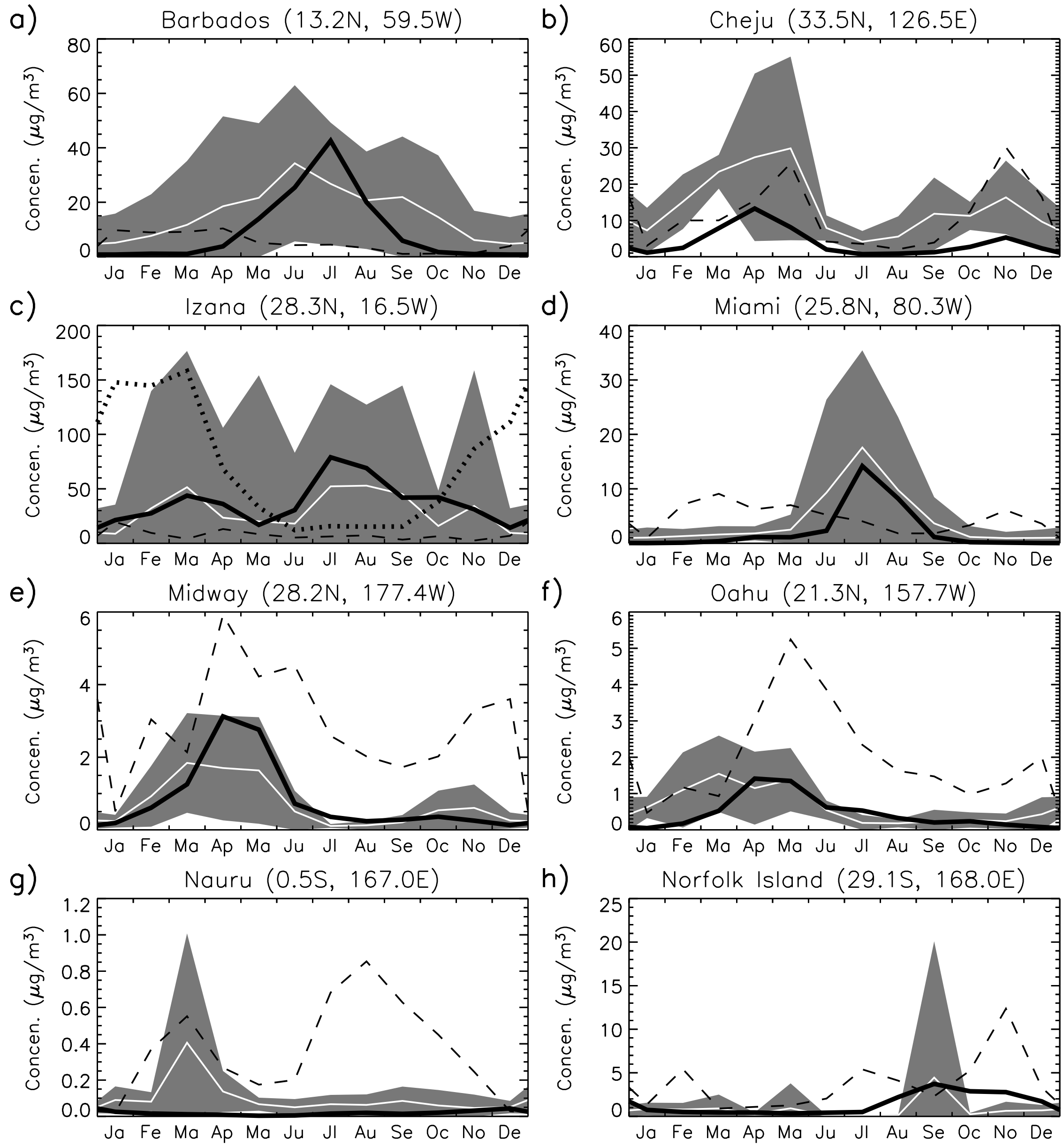

Figure 7. As in Figure 5, but for University of Miami measurements of surface concentration. At Izaña, the model concentration at 2500 m is plotted to correspond to the altitude of the observing station. The dotted line shows model concentration at sea level.

[36] To compare different model versions, we evaluate each model with the same observations used to evaluate the baseline experiment. Given our uncertainty in the coefficients C and $F(r)$ that relate wind speed to emission, we derive separate values for each model version that results in optimal agreement with the observations, as we did for the baseline case. This allows us to compare the optimal version of each model. To see the effect of changing the model, we examine the total error defined in section 2, along with its contribution from each data set, as shown in Figure 11. We compare the fidelity of different model versions using global error as a criterion, but note that models with similar errors may exhibit regional differences.

[37] Comparing the error among different versions of the model raises the question of what represents a large difference. The error for any particular model depends upon not only its intrinsic quality, but also upon whether the five-year averaging period is sufficient to estimate the climatology. To calculate the effect of averaging, we integrated the baseline model for ten years, as described in section 2. We then formed averages from all 252 possible combinations of five year subsets, and found the optimal solution and total error for each. The average total error is 0.52 ± 0.007 (Figure 11a). For comparison, the total error rises to 0.65 (the 'all' case in *Cakmur et al.* [2006]), when calculated using a larger set of measurement locations. Thus, the uncertainty resulting from our five-year averaging period is small compared to that arising from our somewhat subjective choice of measurement locations. In general, we regard differences in model error conservatively by emphasizing the outliers.

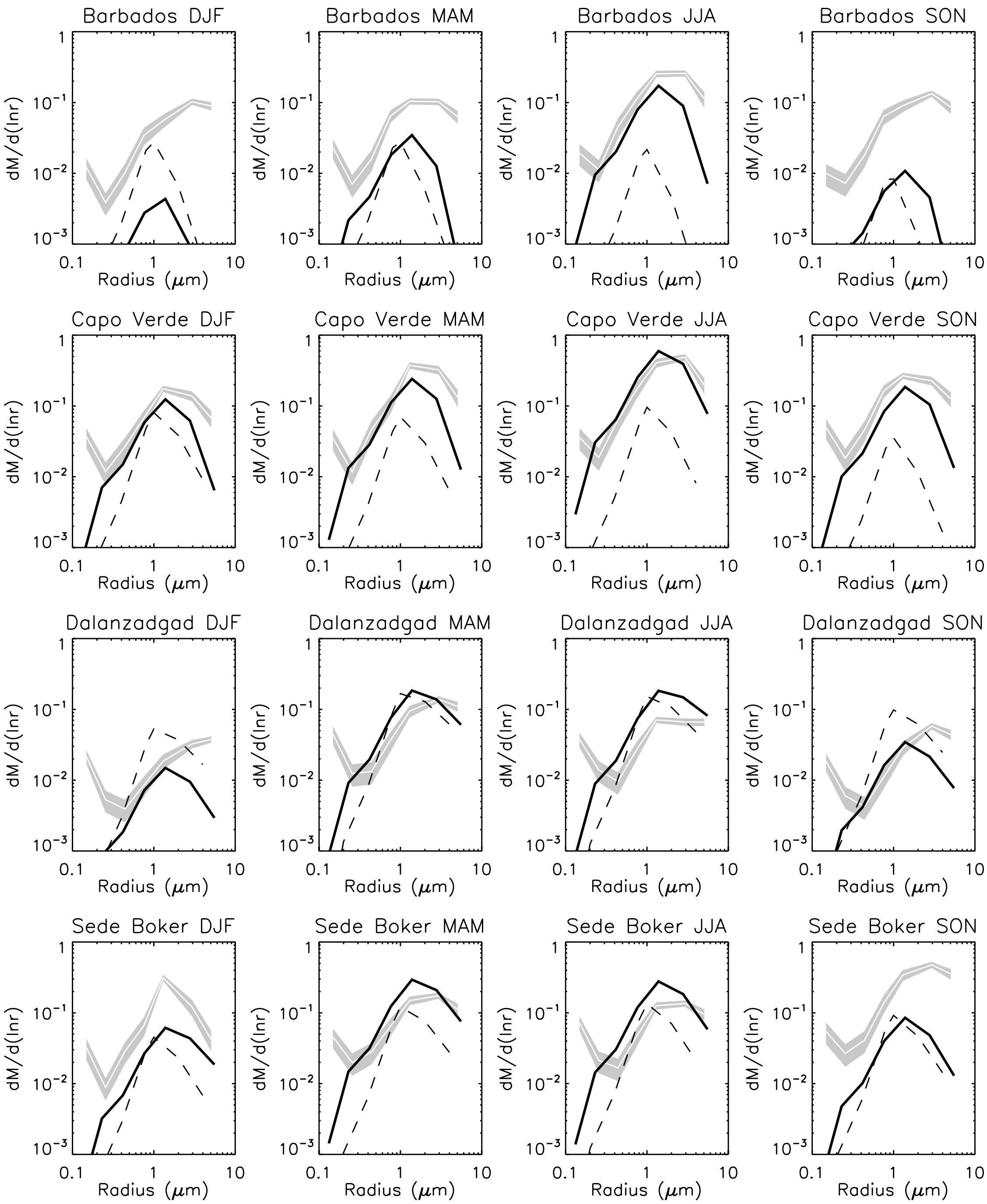

Figure 8. Comparison of baseline experiment (solid black) and GACP (dashed) size distribution to the value retrieved by AERONET (white). Shading represents the error estimated by *Dubovik et al.* [2002] ranging from 10% at the distribution peak to 35% at the minimum.

[38] In the baseline experiment, regions vulnerable to wind erosion are identified by their low surface roughness, based upon monthly averages of the ERS roughness retrieval. As an alternative to using the ERS retrieval to identify ground cover that inhibits dust emission, we replace it with a global inventory of vegetation in experiment B4. Following *Tegen and Miller* [1998], we allow emission only in the grid box fraction corresponding to the grassland, shrub, and bare soil categories in the *Matthews* [1983] data set. The ERS retrieval might seem preferable as a more direct measurement of ground cover. For example, a shrub that loses its leaves during the winter has a smaller roughness and offers less protection from wind erosion during this season, even if its vegetation category is unchanged. Nonetheless, experiment B4 results in a total error that is nearly identical to the baseline case. This similarity is fortunate for modelers wishing to simulate dust in other climates like that of the Last Glacial Maximum, where roughness retrievals are not available but vegetation can be reconstructed.

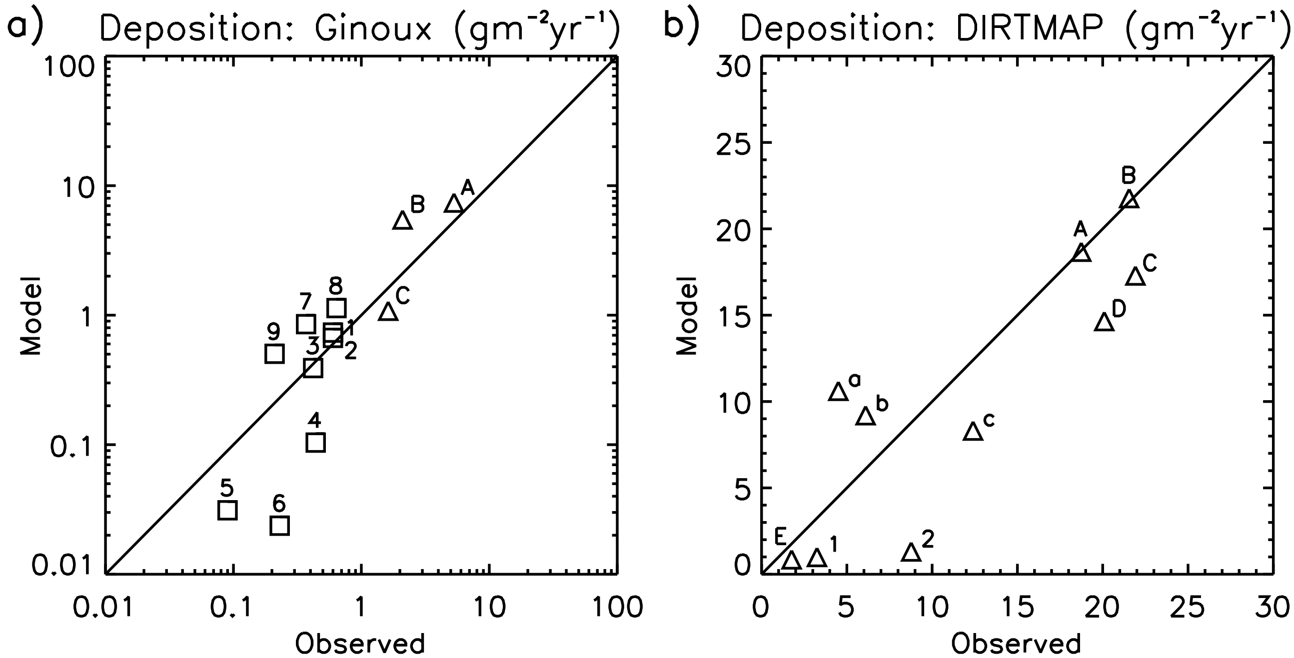

Figure 9. Comparison of baseline experiment deposition ($gm^{-2}yr^{-1}$) to measurements. (a) Deposition compiled by *Ginoux et al.* [2001]. Atlantic measurements (triangles) are ordered according to distance downwind from African sources: A, Spain (2.3°E, 41.8°N); B, French Alps (6.5°E, 45.5°N); and C, Miami (80.3°W, 25.8°N). The numbers denoting Pacific measurements (squares) increase with distance downwind of Asian sources. 1, Midway (177.4W°E, 28.2°N); 2, Shemya (174.1°E, 52.9°N); 3, Oahu (157.6°W, 21.3°N); 4, Enewetak (162.3°E, 11.3°N); 5, Fanning (159.3°W, 3.9°N); 6, Nauru (167.0°E, 0.5°S). Measurements influenced predominately by Australian sources include 7, New Caledonia (167°E, 22.2°S); 8, Norfolk Island (168.0°E, 29.1°S); 9, Rarotonga (159.8°E, 21.3°S). (b) Deposition compiled by DIRTMAP. Uppercase letters correspond to the Atlantic Ocean: A, 21.08°W, 18.50°N; B, 20.17°W, 19.00°N; C, 19.75°W, 20.92°N; D, 20.68°W, 21.15°N; and E, 21.98°W, 33.15°N. Lowercase corresponds to the Indian Ocean: a, 61.50°E, 15.98°N; b, 60.47°E, 16.25°N; and c, 58.80°E, 17.40°N. Numbers correspond to the Pacific Ocean: 1, 177.74°E, 34.42°N; and 2, 174.95°E, 37.40°N.

[39] *Tegen et al.* [2002] find that model emission over the Gobi and Taklimakan during NH spring prior to the appearance of grass is decreased when the seasonal cycle of vegetation is removed. In contrast, *Luo et al.* [2003] calculate reasonable long-range transport of dust to the Pacific without accounting for this cycle. As an alternative to prescribed monthly variations of surface roughness, we prescribe its annual average in experiment B1. The total error and optimal emission are hardly changed, at least globally, as indicated by Figures 11 and 12. To see the

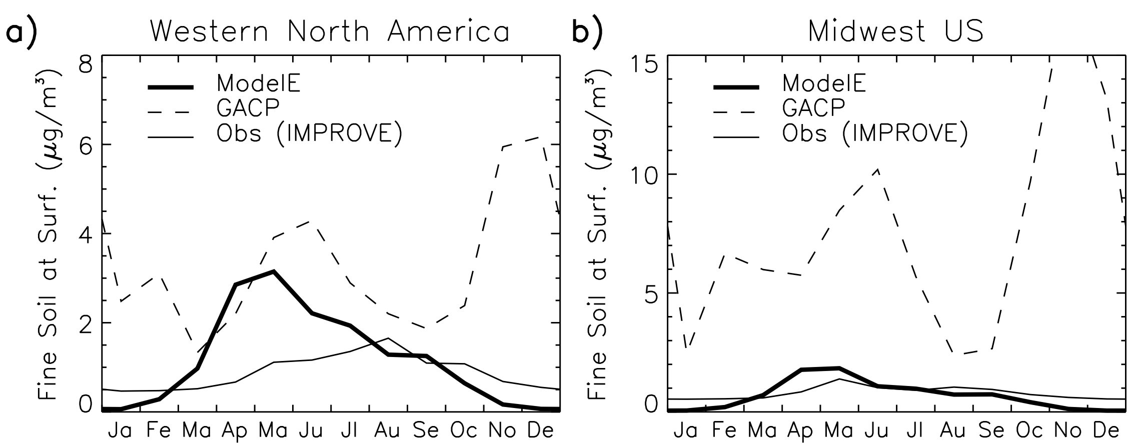

Figure 10. Annual cycle of surface concentration of fine soil (radius <1.25 μm) according to the baseline (thick solid) and GACP distributions (dashed), and measured by the IMPROVE stations (thin solid) listed in Table 2. (a) Western North America (120–105°W, 28–44°N); (b) Midwest North America (105–100°W, 28–44°N).

Table 2. N.P., National Park; N.M., National Monument; S.P., State Park

Location	ID	Longitude	Latitude
	Figure 10a: Western North America		
Bandelier N.M.	band1	106.3W	35.8N
Bliss S.P.	blis1	120.1W	39.0N
Bryce Canyon N.P.	brca1	112.2W	37.6N
Bridger Wilderness	brid1	109.8W	43.0N
Canyonlands N.P.	cany1	109.8W	38.5N
Chiricahua N.M.	chir1	109.4W	32.0N
Gila Cliff Dwellings N.P.	gicl1	108.2W	33.2N
Great Basin N.P.	grba1	114.2W	39.0N
Great Sand Dunes N.M.	grsa1	105.5W	37.7N
Jarbidge Wilderness	jarb1	115.4W	41.9N
Lone Peak Wilderness	lope1	111.7W	40.4N
Mesa Verde N.P.	meve1	108.5W	37.2N
Mount Zirkel Wilderness	mozi1	106.7W	40.5N
Petrified Forest N.P.	pefo1	109.8W	35.1N
Rocky Mountain N.P.	romo1	105.6W	40.3N
San Gorgonio N.P.	sago1	116.9W	34.2N
Sequoia N.P.	sequ1	118.8W	36.5N
Tonto N.M.	tont1	111.1W	33.7N
Weminuche Wilderness	wemi1	107.8W	37.7N
Yellowstone N.P.	yell2	110.4W	44.6N
Yosemite N.P.	yose1	119.7W	37.7N
	Figure 10b: Midwest		
Badlands N.P.	badl1	101.9W	43.7N
Big Bend N.P.	bibe1	103.2W	29.3N
Guadalupe Mountains N.P.	gumo1	104.8W	31.8N

effect of annual roughness variations upon regional emission, we removed the annual cycle as in experiment B1, but without reoptimizing the model. The absence of an annual cycle decreases emission over the Taklimakan by 18%, which is somewhat offset by a 12% increase over the Gobi desert, in contrast to the decrease over both regions found by *Tegen et al.* [2002]. Our use of roughness may underestimate the effect of seasonal variations of vegetation if grass inhibits dust emission by anchoring soil particles through its roots rather than absorbing the force of the wind.

[40] In experiments B2 and B3, we make the roughness criterion for emission more or less stringent, respectively. (In experiment B2, the threshold roughness is reduced by a factor of five, which reduces the number of potential emitting sites; in B3, it is doubled.) Again the error is barely changed relative to the baseline case. In contrast to our use of a globally uniform roughness that is a threshold for emission, *Prigent et al.* [2005] introduce geographic variations in the wind stress threshold for emission according to the retrieved roughness [cf. *Marticorena and Bergametti*, 1995], improving their model agreement with the TOMS aerosol index over the Sahara. At present, we neglect these variations, although the insensitivity of our global error in experiments B2 and B3 suggests that variations in the wind stress threshold

Table 3. Summary of Experiments

Experiment	Description
A	Baseline[a]
B1	Replace monthly ERS retrieval with annual average
B2	More stringent ERS threshold for emission (from −13 to −18 dB)
B3	Less stringent ERS threshold for emission (from −13 to −11 dB)
B4	Replace ERS roughness criterion with *Matthews* [1983] vegetation
B5	Neither ERS roughness criterion nor *Matthews* [1983] vegetation
B6	Neither ERS roughness criterion nor *Matthews* [1983] vegetation nor *Ginoux et al.* [2001] preferred source
C1	Make w_T more sensitive to soil wetness q: $w_T = w_{T,0}\ \exp(1.0\ q)$
C2	Replace Fecan/Shao threshold dependence upon soil wetness q with duration of positive $E - P$ [*Tegen and Miller*, 1998]
E	Remove subgrid distribution of wind speed (w_T = 4 m/s)
F	Remove *Ginoux et al.* [2001] preferred sources
G	Replace *Sinyuk et al.* [2003] with *Patterson et al.* [1977] index of refraction
H	Specify clay and silt availability
CMTo	*Cakmur et al.* [2004]: old model with subgrid distribution of wind speed
TM98	Old model [*Tegen and Miller*, 1998] w/ 1300 Tg global annual emission
TM98o	Old model [*Tegen and Miller*, 1998] w/ optimal emission
GACP	Distribution derived from offline tracer model [*Tegen et al.*, 1997]

[a]In the baseline experiment, emission occurs in the fraction of each AGCM grid box where the ERS roughness retrieval falls below −13 dB and abundant erodible particles are identified by the *Ginoux et al.* [2001] preferred source. The wind speed threshold increases with soil wetness q according to $w_T = w_{T,0}\ \exp(0.7\ q)$ where $w_{T,0}$ equals 8 ms^{-1}. Subgrid wind fluctuations are parameterized as in *Cakmur et al.* [2004]. Solar absorption is taken from *Sinyuk et al.* [2003]. The magnitude of clay and silt emission is derived a posteriori, so that the dust cycle agrees optimally with the observations.

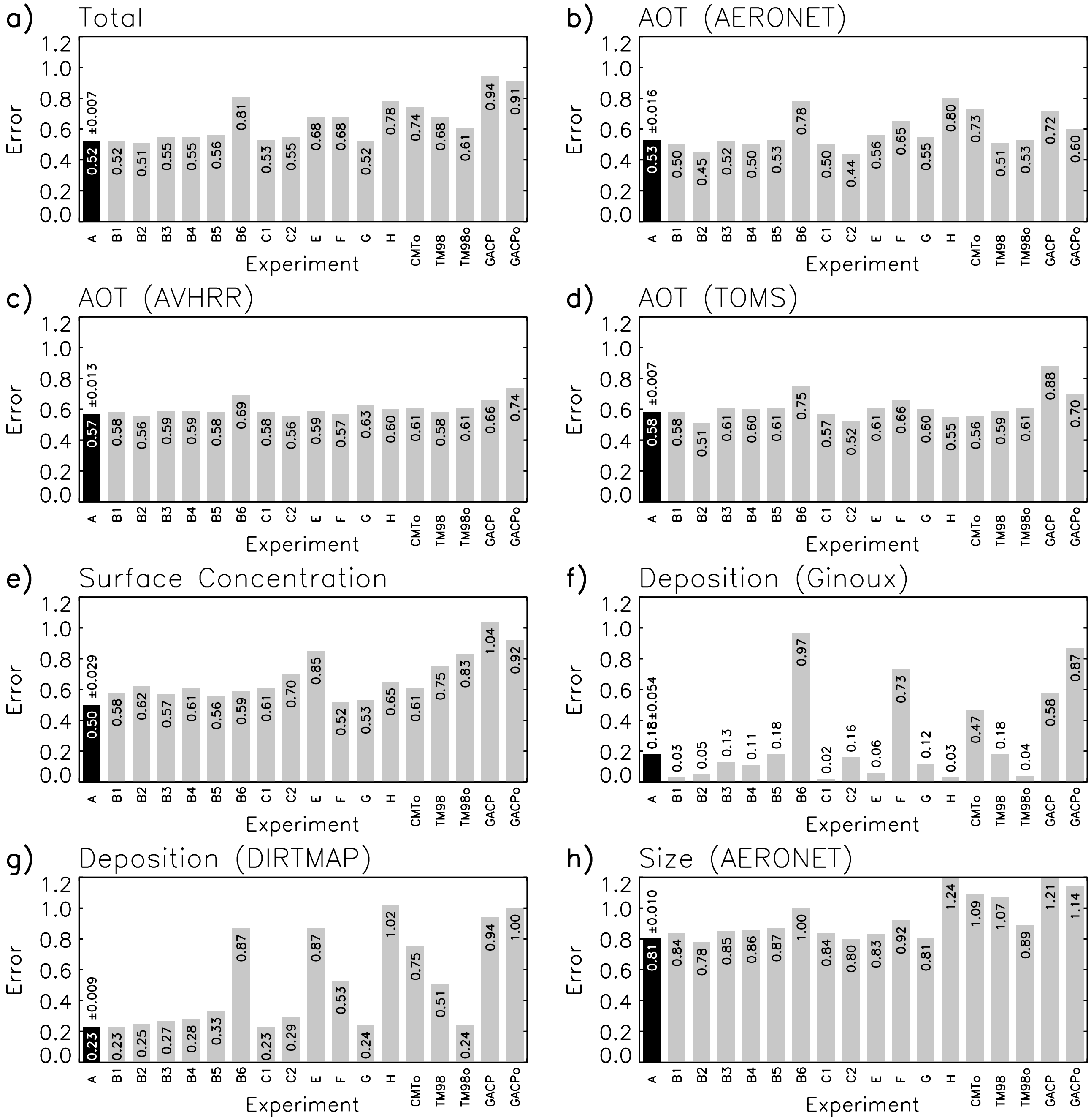

Figure 11. Total error and contribution from each data set for each sensitivity experiment described in Table 3.

may concentrate emission to a few locations without changing the total emission from major source regions and the agreement of the emitted dust with observations downwind.

[41] Inhibition of wind erosion by soil moisture in the baseline model occurs through an increase in the wind speed threshold for emission. In experiment C1, we increased the threshold sensitivity to soil moisture by about 50% and found that this has little effect upon the dust distribution. In *Tegen and Miller* [1998], this binding effect is represented by allowing emission to occur only when evaporation exceeds precipitation for a prescribed duration. Reintroducing this parameterization in experiment C2, also had little effect upon the distribution.

[42] In experiment B5, we impose neither a roughness nor vegetation criterion, allowing dust to be emitted in any topographic depression identified by *Ginoux et al.* [2001] where the soil is sufficiently dry. The total error is nearly unchanged. While *Ginoux et al.* [2001] prohibit emission where vegetation is abundant, the distribution of topographic depressions by itself seems sufficient to determine emission. Only when both the vegetation and topography criteria are removed, as in experiment B6, so that the potential for emission is determined solely by soil mois-

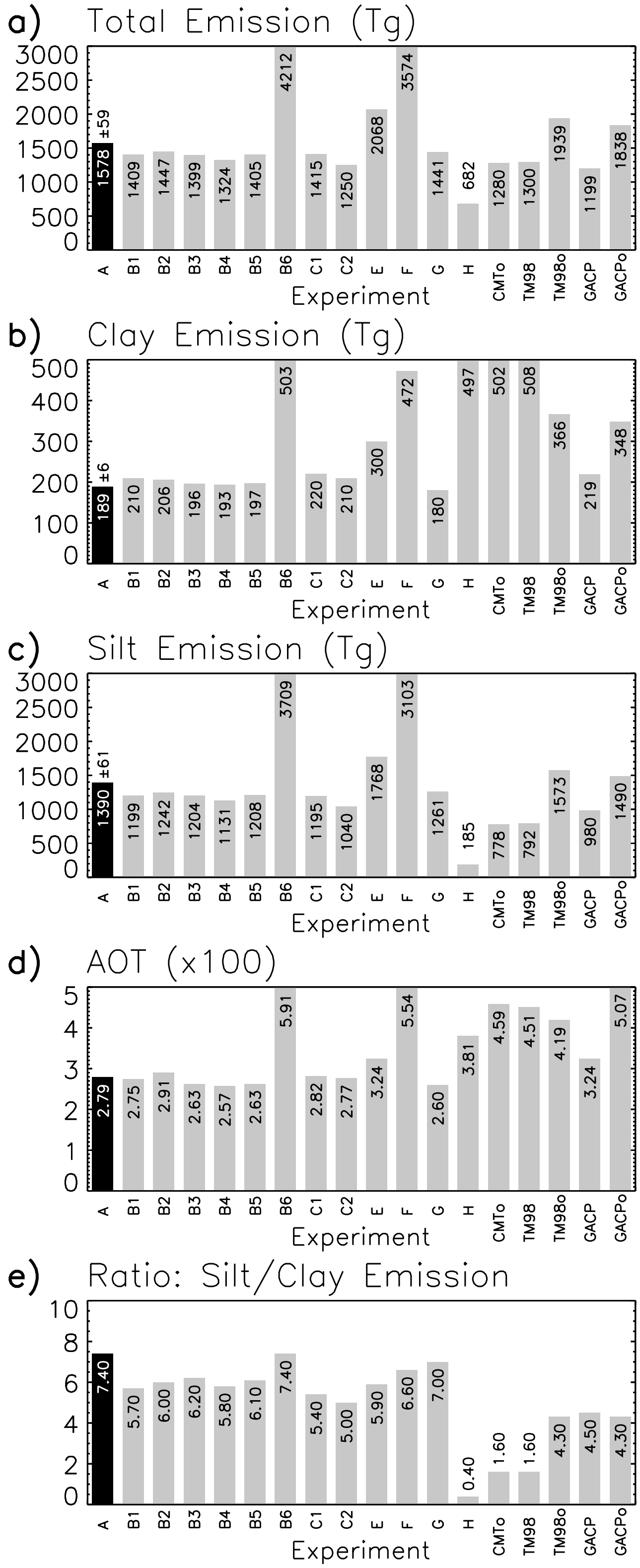

Figure 12. (a) Emission including the contribution from (b) clay and (c) silt (Tg), along with (d) clear-sky optical thickness and (e) the ratio of silt to clay emission for each sensitivity experiment described in Table 3.

ture, does the quality of the simulation markedly degrade (Figure 11). Experiment B6 suggests that simulation of realistic emission depends upon knowledge of where erodible soil particles are abundant, in this case given by a topographic criterion. Limited soil moisture by itself does not create the potential for dust emission, except through its inhibition of vegetation.

[43] Absorption of solar radiation by dust is reduced by roughly two-thirds in the baseline model, compared to the absorption used in the previous model that is based upon measurements by *Patterson et al.* [1977]. When this greater absorption is reintroduced to calculate the AOT (experiment G), the total error remains nearly identical, although the AOT error increases slightly. (Because dust radiative forcing is not allowed to perturb the climate, the effect of increasing absorption is only to change the AOT that is compared to observations.) Whether the laboratory measurements of *Patterson et al.* [1977] or the retrievals from in situ measurements by *Sinyuk et al.* [2003] are more appropriate is not determined by the combination of our model and these data sets.

[44] The total error of our baseline model is substantially lower than that of our previous model [*Tegen and Miller*, 1998]. Assuming global, annual emission of 1300 Tg [*Perlwitz et al.*, 2001], the total error of the latter is 0.68 (experiment TM98), although this can be reduced to 0.61 if the global, annual emission is increased through optimization to over 1900 Tg (experiment TM98o). In either case, this is larger than the total error of 0.52 for the baseline case. Note that the silt fraction of emission is markedly reduced in the previous model (Figure 12e).

[45] Comparison of experiments TM98 and TM98o to the baseline raises the question of which changes contribute most to the more accurate simulation by the baseline model. Reintroduction into the baseline model of the vegetation criterion (B4), along with former versions of the soil moisture criterion (C2), and solar absorption (G) from *Tegen and Miller* [1998] has little effect upon the optimal dust distribution and total error. In contrast, removal of either the subgrid distribution of surface wind speed (experiment E) or the preferred source (experiment F) increases the total error to 0.68. The increased error suggests that the main contributions to the improvement of the baseline model are the subgrid wind parameterization and representation of preferred sources in combination. However, addition of the subgrid parameterization to the previous model (experiment CMTo), as in *Cakmur et al.* [2004], increases the total error to 0.74, suggesting that the model behavior is non-linear. The effect of the subgrid parameterization is dependent upon the model to which it is added or removed.

[46] The total error of the baseline simulation is also increased if the globally uniform clay and silt availability $F(r)$, derived a posteriori through optimization, are replaced by geographically varying values taken from the *Zobler* [1986] atlas (experiment H). This atlas was derived for agricultural purposes and may not represent the soil texture in environments like dry lake beds that are preferred sources for dust. However, it is important to note that our optimal values of clay and silt availability in the baseline model have no physical basis, and are simply tuned to maximize agreement of the model's dust cycle with observations.

Ideally, global measurements of the soil particle size distribution for each dust source would be available to modelers.

[47] Finally, we compare the baseline and the GACP distribution described in section 2. The total error of the GACP distribution is 0.94, which is high compared to the baseline value, and is only slightly improved to 0.91 by optimizing the clay and silt emission (Figures 11 and 12). The comparison is shown for AOT, surface concentration, and size in Figures 5–8 and Figure 10. (The GACP distribution is marked as a dashed line.) Over Asia, the two distributions are similar, although the GACP overestimates the surface concentration over the Pacific. The two distributions are also similar over Arabia and Australia. The largest improvement by the baseline model is over the Atlantic during NH summer. Over the Sahara, and downwind toward the Caribbean, the baseline model is in better agreement with the observations, with a greater AOT and surface concentration. The baseline model also comes closer to matching the IMPROVE measurements of surface concentration over North America.

5. Conclusions

[48] By comparing to data sets ranging from AOT and surface concentration to deposition and aerosol size distribution, we show that the new model of the dust aerosol cycle results in a more realistic distribution of dust than that calculated either by a prior version of the AGCM [*Tegen and Miller*, 1998] or an offline tracer model (GACP). This improvement is noteworthy because tuning was much more extensive in the previous AGCM, where the wind speed threshold for emission was adjusted at each grid box to match observations of surface concentration. The improvement is largest for the Sahara and downwind over the Atlantic and Caribbean during NH summer, where the model dust transport is of realistic magnitude. However, observations suggest that model deposition is too efficient in this region, especially during NH winter, partly as a result of AGCM rainfall errors.

[49] The most significant improvement to the new model results from the introduction of a subgrid distribution of surface wind speed and 'preferred sources' as defined by *Ginoux et al.* [2001]. Consistent with the results of *Cakmur et al.* [2004], the subgrid wind distribution increases summertime emission over deserts like the Sahara, where intense solar heating of the surface causes wind speed fluctuations associated with convective mixing. Removal of the subgrid wind parameterization from the baseline model leads to a substantially larger total error. However, we also found that adding the subgrid wind distribution to the previous model actually causes a slight increase in the total error (although *Cakmur et al.* [2004] show that the agreement with observed AOT improves over the Sahara and Taklimakan). That the effect of the subgrid wind parameterization depends strongly upon the model to which it is added demonstrates the non-linear behavior of the AGCM dust cycle.

[50] While the global error is less sensitive to other changes to the model, these changes cause regional differences that we do not discuss here. We also note that the error is influenced by our subjective choice of data sets and measurement locations, as explored in more detail by our companion article [*Cakmur et al.*, 2006]. We have tried to minimize the error sensitivity to a particular observation by comparing to a large number of measurements at a worldwide array of stations. We have also emphasized only the model features that cause the greatest reduction in error and model improvement.

[51] Dust transport and removal is now represented in the ModelE AGCM using the same physics as other aerosol species. The exception is for wet deposition of dust, which in these experiments is calculated using a single scavenging coefficient, as in *Tegen and Fung* [1994]. Dust particles can be made hydrophilic and nucleate cloud droplets through heterogeneous chemistry and uptake of pollutants on the particle surface [*Jordan et al.*, 2003; *Arimoto et al.*, 2004; *Bauer and Koch*, 2005]. We intend to distinguish between collisional and nucleation scavenging by modifying parameterizations that have been developed for other aerosols in the AGCM. We also plan to take advantage of the new ERS scatterometer retrievals of surface roughness to compute their effect upon the wind threshold [*Marticorena and Bergametti*, 1995; *Prigent et al.*, 2005].

[52] The dust model will be included in the next release of the ModelE AGCM, along with an option to use the pre-calculated dust distribution derived from the baseline experiment.

[53] **Acknowledgments.** This article was improved by the comments of Natalie Mahowald and an anonymous reviewer. We thank the AERONET PI's for use of their observations: Mary Jane Bartholomew, Brent Holben, Chuck McClain, Ross Mitchell, Didier Tanré, John Vande Castle, and Jeannette Vandenbosch. We are also grateful to Omar Torres for use of the TOMS AOT, along with Joseph Prospero and Dennis Savoie at the University of Miami for their measurements of concentration. This article benefited from comments by Oleg Dubovik and Michael Mishchenko. This work was supported by the Climate Dynamics Program of the National Science Foundation through ATM-01-24258. R.V.C. thanks Tsengdar Lee and Don Anderson of the NASA Atmospheric Modeling Program for additional support through the National Research Council.

References

Alfaro, S. C., and L. Gomes (2001), Modeling mineral aerosol production by wind erosion: Emission intensities and aerosol size distributions in source areas, *J. Geophys. Res.*, *106*, 18,075–18,084.

Andreae, M. O. (1995), Climatic effects of changing atmospheric aerosol levels, in *Future Climates of the World: A Modelling Perspective, World Survey of Climatology*, vol. 16, edited by A. Henderson-Sellers, pp. 347–398, Elsevier, New York.

Arimoto, R., X. Y. Zhang, B. J. Huebert, C. H. Kang, D. L. Savoie, J. M. Prospero, S. K. Sage, C. A. Schloesslin, H. M. Khaing, and S. N. Oh (2004), Chemical composition of atmospheric aerosols from Zhenbeitai, China, and Gosan, South Korea, during ACE-Asia, *J. Geophys. Res.*, *109*, D19S04, doi:10.1029/2003JD004323.

Bauer, S. E., and D. Koch (2005), Impact of heterogeneous reactions between sulfate and mineral dust aerosols on climate in the GISS GCM, *J. Geophys. Res.*, *110*, D17202, doi:10.1029/2005JD005870.

Cakmur, R., R. L. Miller, and O. Torres (2004), Incorporating the effect of small-scale circulations upon dust emission in an atmospheric general circulation model, *J. Geophys. Res.*, *109*, D07201, doi:10.1029/2003JD004067.

Cakmur, R. V., R. L. Miller, J. Perlwitz, I. V. Geogdzhayev, P. Ginoux, D. Koch, K. E. Kohfeld, I. Tegen, and C. S. Zender (2006), Constraining the magnitude of the global dust cycle by minimizing the difference between a model and observations, *J. Geophys. Res.*, *111*, D06207, doi:10.1029/2005JD005791.

Carlson, T. N., and J. M. Prospero (1972), The large-scale movement of Saharan air outbreaks over the northern equatorial Atlantic, *J. Appl. Meteorol.*, *11*, 283–297.

Charlson, R. J., S. E. Schwarz, J. M. Hales, R. D. Cess, J. A. Coakley, J. E. Hansen, and D. J. Hofmann (1992), Climate forcing by anthropogenic aerosols, *Science*, *255*, 423–430.

Cheng, Y., V. M. Canuto, and A. M. Howard (2002), An improved model for the turbulent PBL, *J. Atmos. Sci.*, *59*, 1550–1565, doi:10.1175/1520-0469(2002)059<1550:AIMFTT>2.0.CO;2.

Cheng, Y., V. M. Canuto, and A. M. Howard (2003), Comments on "An improved model for the turbulent PBL", *J. Atmos. Sci.*, *60*, 3043–3046, doi:10.1175/1520-0469(2003)060<3043:COOAIM>2.0.CO;2.

Cheng, Y., V. M. Canuto, and A. M. Howard (2004), Reply to "Comments on an improved model for the turbulent PBL" by Hassid and Galperin, *J. Atmos. Sci.*, *61*, 1200–1204, doi:10.1175/1520-0469(2004)061<1200:R>2.0.CO;2.

Chu, D. A., Y. J. Kaufman, C. Ichoku, L. A. Remer, D. Tanré, and B. N. Holben (2002), Validation of MODIS aerosol optical depth retrieval over land, *Geophys. Res. Lett.*, *29*(12), 8007, doi:10.1029/2001GL013205.

Colarco, P. R., O. B. Toon, O. Torres, and P. J. Rasch (2002), Determining the UV imaginary index of refraction of Saharan dust particles from Total Ozone Mapping Spectrometer data using a three-dimensional model of dust transport, *J. Geophys. Res.*, *107*(D16), 4289, doi:10.1029/2001JD000903.

Dubovik, O., B. N. Holben, T. F. Eck, A. Smirnov, Y. J. Kaufman, M. D. King, D. Tanré, and I. Slutsker (2002), Variability of absorption and optical properties of key aerosol types observed in worldwide locations, *J. Atmos. Sci.*, *59*, 590–608.

Dufresne, J.-L., C. Gautier, and Y. Fouquart (2002), Longwave scattering effects of mineral aerosols, *J. Atmos. Sci.*, *59*, 1959–1966.

Engelstaedter, S., K. E. Kohfeld, I. Tegen, and S. P. Harrison (2003), Controls on dust emissions by vegetation and topographic depressions: An evaluation using dust storm frequency data, *Geophys. Res. Lett.*, *30*(6), 1294, doi:10.1029/2002GL016471.

Fecan, F., B. Marticorena, and G. Bergametti (1999), Parameterization of the increase of the aeolian erosion threshold wind friction velocity due to soil moisture for arid and semi-arid areas, *Ann. Geophys.*, *17*, 149–157.

Gillette, D. A. (1974), On the production of soil wind erosion aerosols having the potential for long-range transport, *J. Rech. Atmos.*, *8*, 735–744.

Gillette, D. A. (1999), A qualitative geophysical explanation for "hot spot" dust emitting source regions, *Contrib. Atmos. Phys.*, *72*, 67–77.

Gillette, D. A., and R. Passi (1988), Modeling dust emission caused by wind erosion, *J. Geophys. Res.*, *93*, 14,233–14,242.

Ginoux, P. (2003), Effects of nonsphericity on mineral dust modeling, *J. Geophys. Res.*, *108*(D2), 4052, doi:10.1029/2002JD002516.

Ginoux, P., M. Chin, I. Tegen, J. Prospero, B. Holben, O. Dubovik, and S. J. Lin (2001), Sources and distributions of aerosols simulated with the GOCART model, *J. Geophys. Res.*, *106*, 20,255–20,273.

Grini, A., and C. S. Zender (2004), Roles of saltation, sandblasting, and wind speed variability on mineral dust aerosol size distribution during the Puerto Rican Dust Experiment, *J. Geophys. Res.*, *109*, D07202, doi:10.1029/2003JD004233.

Grini, A., C. S. Zender, and P. R. Colarco (2002), Saltation sandblasting behavior during mineral aerosol production, *Geophys. Res. Lett.*, *29*(18), 1868, doi:10.1029/2002GL015248.

Grini, A., G. Myhre, C. S. Zender, and I. S. A. Isaksen (2005), Model simulations of dust sources and transport in the global atmosphere: Effects of soil erodibility and wind speed variability, *J. Geophys. Res.*, *110*, D02205, doi:10.1029/2004JD005037.

Hansen, J. E., and M. Sato (2001), Trends of measured climate forcing agents, *Proc. Natl. Acad. Sci.*, *98*, 14,778–14,783, doi:10.1073/pnas.261553698.

Hansen, J. E., et al. (2002), Climate forcings in Goddard Institute for Space Studies SI2000 simulations, *J. Geophys. Res.*, *107*(D18), 4347, doi:10.1029/2001JD001143.

Herman, J. R., P. K. Bhartia, O. Torres, C. Hsu, C. Seftor, and E. Celarier (1997), Global distribution of UV-absorbing aerosols from Nimbus-7/TOMS data, *J. Geophys. Res.*, *102*, 16,911–16,922.

Holben, B. N., et al. (2001), An emerging ground-based climatology: Aerosol optical depth from AERONET, *J. Geophys. Res.*, *106*, 12,067–12,097.

Idso, S. B., R. S. Ingram, and J. M. Pritchard (1972), An American Haboob, *Bull. Am. Meteorol. Soc.*, *53*, 930–935.

Iversen, J. D., and B. R. White (1982), Saltation threshold on Earth, Mars and Venus, *Sedimentology*, *29*, 111–119.

Jordan, C. E., J. E. Dibb, B. E. Anderson, and H. E. Fuelberg (2003), Uptake of nitrate and sulfate on dust aerosols during TRACE-P, *J. Geophys. Res.*, *108*(D21), 8817, doi:10.1029/2002JD003101.

Justus, C., and A. Mikhail (1976), Height variation of wind speed and wind distributions statistics, *Geophys. Res. Lett.*, *3*, 261–264.

Kahn, R. A., B. J. Gaitley, J. V. Martonchik, D. J. Diner, K. A. Crean, and B. Holben (2005), Multiangle Imaging Spectroadiometer MISR global aerosol optical depth validation based on 2 years of coincident Aerosol Robotic Network AERONET observations, *J. Geophys. Res.*, *110*, D10S04, doi:10.1029/2004JD004706.

Karyampudi, V. M., and T. N. Carlson (1988), Analysis and numerical simulation of the Saharan Air Layer and its effect upon easterly wave disturbances, *J. Atmos. Sci.*, *45*, 3102–3136.

Kaufman, Y. J., D. Tanré, O. Dubovik, A. Karnieli, and L. A. Remer (2001), Absorption of sunlight by dust as inferred from satellite and ground-based remote sensing, *Geophys. Res. Lett.*, *28*, 1479–1482.

Koch, D., D. Jacob, I. Tegen, D. Rind, and M. Chin (1999), Tropospheric sulfur simulation and sulfate direct radiative forcing in the Goddard Institute for Space Studies general circulation model, *J. Geophys. Res.*, *104*, 23,799–23,822.

Koch, D., G. A. Schmidt, and C. Field (2006), Sulfur, sea salt and radionuclide aerosols in GISS ModelE, *J. Geophys. Res.*, doi:10.1029/2004JD005550, in press.

Kohfeld, K., and S. P. Harrison (2001), DIRTMAP: The geologic record of dust, *Earth Sci. Rev.*, *54*, 81–114.

Luo, C., N. M. Mahowald, and J. del Corral (2003), Sensitivity study of meteorological parameters on mineral aerosol mobilization, transport, and distribution, *J. Geophys. Res.*, *108*(D15), 4447, doi:10.1029/2003JD003483.

Mahowald, N., and C. Luo (2003), A less dusty future?, *Geophys. Res. Lett.*, *30*(17), 1903, doi:10.1029/2003GL017880.

Mahowald, N. M., G. D. R. Rivera, and C. Luo (2004), Comment on "Relative importance of climate and land use in determining present and future global soil dust emission" by I. Tegen et al., *Geophys. Res. Lett.*, *31*, L24105, doi:10.1029/2004GL021272.

Malm, W. C., J. F. Sisler, D. Huffman, R. A. Eldred, and T. A. Cahill (1994), Spatial and seasonal trends in particle concentrations and optical extinction in the United States, *J. Geophys. Res.*, *99*, 1347–1370.

Marticorena, B., and G. Bergametti (1995), Modeling the atmospheric dust cycle: 1. Design of a soil-derived dust emission scheme, *J. Geophys. Res.*, *100*, 16,415–16,430.

Matthews, E. (1983), Global vegetation and land use: New high-resolution databases for climate studies, *J. Clim. Appl. Meteorol.*, *22*, 474–487.

Miller, R. L., J. Perlwitz, and I. Tegen (2004a), Feedback by dust radiative forcing upon dust emission through the planetary boundary layer, *J. Geophys. Res.*, *109*, D24209, doi:10.1029/2004JD004912.

Miller, R. L., J. Perlwitz, and I. Tegen (2004b), Modeling Arabian dust mobilization during the Asian summer monsoon: The effect of prescribed versus calculated SST, *Geophys. Res. Lett.*, *31*, L22214, doi:10.1029/2004GL020669.

Miller, R. L., I. Tegen, and J. Perlwitz (2004c), Surface radiative forcing by soil dust aerosols and the hydrologic cycle, *J. Geophys. Res.*, *109*, D04203, doi:10.1029/2003JD004085.

Mishchenko, M., A. Lacis, B. Carlson, and L. Travis (1995), Nonsphericitiy of dust-like tropospheric aerosols: Implications for aerosol remote sensing and climate, *Geophys. Res. Lett.*, *22*, 1077–1080.

Mishchenko, M. I., I. V. Geogdzhayev, B. Cairns, W. B. Rossow, and A. A. Lacis (1999), Aerosol retrievals over the ocean by use of channels 1 and 2 AVHRR data: Sensitivity analysis and preliminary results, *Appl. Opt.*, *38*, 7325–7341.

Patterson, E. M., D. A. Gillette, and B. H. Stockton (1977), Complex index of refraction between 300 and 700 nm for Saharan aerosols, *J. Geophys. Res.*, *82*, 3153–3160.

Pavia, E., and J. O'Brien (1986), Weibull statistics of wind speed over the ocean, *J. Clim. Appl. Meteorol.*, *25*, 1324–1332.

Penner, J. E., et al. (2001), Aerosols, their direct and indirect effects, in *Climate Change 2001: The Scientific Basis. Contribution of Working Group I to the Third Assessment Report of the Intergovernmental Panel on Climate Change*, edited by J. Houghton et al., pp. 289–348, Cambridge Univ. Press, New York.

Perlwitz, J., I. Tegen, and R. L. Miller (2001), Interactive soil dust aerosol model in the GISS GCM: 1. Sensitivity of the soil dust cycle to radiative properties of soil dust aerosols, *J. Geophys. Res.*, *106*, 18,167–18,192.

Prather, M. (1986), Numerical advection by conservation of second-order moments, *J. Geophys. Res.*, *91*, 6671–6680.

Prigent, C., I. Tegen, F. Aires, B. Marticorena, and M. Zribi (2005), Estimation of the aerodynamic roughness length in arid and semi-arid regions over the globe with the ERS scatterometer, *J. Geophys. Res.*, *110*, D09205, doi:10.1029/2004JD005370.

Prospero, J. (1996), The atmospheric transport of particles to the ocean, in *Particle Flux in the Ocean*, edited by V. Ittekkot, P. Schäfer, S. Honjo, and P. J. Depetris, chap. 3, pp. 19–56, John Wiley, Hoboken, N. J.

Prospero, J. M., P. Ginoux, O. Torres, and S. Nicholson (2002), Environmental characterization of global sources of atmospheric soil dust derived from NIMBUS-7 TOMS absorbing aerosol product, *Rev. Geophys.*, *40*(1), 1002, doi:10.1029/2000RG000095.

Ramanathan, V., P. J. Crutzen, J. T. Kiehl, and D. Rosenfeld (2001), Aerosols, climate, and the hydrologic cycle, *Science*, *294*, 2119–2124.

Rennó, N. O., M. L. Burkett, and M. P. Larkin (1998), A simple thermodynamical theory for dust devils, *J. Atmos. Sci.*, *55*, 3244–3252.
Schmidt, G. A., et al. (2006), Present day atmospheric simulations using GISS modelE: Comparison to in-situ, satellite and reanalysis data, *J. Clim.*, *19*, 153–192.
Seinfeld, J. H., et al. (2004), ACE-ASIA: Regional climatic and atmospheric chemical effects of Asian dust and pollution, *Bull. Am. Meteorol. Soc.*, *85*(3), 367–380.
Shao, Y. (2001), A model for mineral dust emission, *J. Geophys. Res.*, *106*, 20,239–20,254.
Shao, Y., M. R. Raupach, and P. A. Findlater (1993), Effect of saltation bombardment on the entrainment of dust by wind, *J. Geophys. Res.*, *98*, 12,719–12,726.
Shao, Y., M. R. Raupach, and J. F. Leys (1996), A model for predicting aeolian sand drift and dust entrainment on scales from paddock to region, *Aust. J. Soil Res.*, *34*, 309–342.
Sinclair, P. C. (1969), General characteristics of dust devils, *J. Appl. Meteorol.*, *8*, 32–45.
Sinclair, P. C. (1973), The lower structure of dust devils, *J. Atmos. Sci.*, *30*, 1599–1619.
Sinyuk, A., O. Torres, and O. Dubovik (2003), Combined use of satellite and surface observations to infer the imaginary part of the refractive index of Saharan dust, *Geophys. Res. Lett.*, *30*(2), 1081, doi:10.1029/2002GL016189.
Sokolik, I., A. Andronova, and T. C. Johnson (1993), Complex refractive index of atmospheric dust aerosols, *Atmos. Environ.*, *27A*, 2495–2502.
Tegen, I., and I. Fung (1994), Modeling of mineral dust in the atmosphere: Sources, transport, and optical thickness, *J. Geophys. Res.*, *99*, 22,897–22,914.
Tegen, I., and A. A. Lacis (1996), Modeling of particle influence on the radiative properties of mineral dust aerosol, *J. Geophys. Res.*, *101*, 19,237–19,244.
Tegen, I., and R. Miller (1998), A general circulation model study on the interannual variability of soil dust aerosol, *J. Geophys. Res.*, *103*, 25,975–25,995.
Tegen, I., P. Hollrig, M. Chin, I. Fung, D. Jacob, and J. Penner (1997), Contribution of different aerosol species to the global aerosol extinction optical thickness: Estimates from model results, *J. Geophys. Res.*, *102*, 23,895–23,915.
Tegen, I., S. P. Harrison, K. Kohfeld, I. C. Prentice, M. Coe, and M. Heimann (2002), Impact of vegetation and preferential source areas on global dust aerosol: Results from a model study, *J. Geophys. Res.*, *107*(D21), 4576, doi:10.1029/2001JD000963.
Tegen, I., M. Werner, S. P. Harrison, and K. E. Kohfeld (2004a), Relative importance of climate and land use in determining present and future global soil dust emission, *Geophys. Res. Lett.*, *31*, L05105, doi:10.1029/2003GL019216.
Tegen, I., M. Werner, S. P. Harrison, and K. E. Kohfeld (2004b), Reply to comment by N. M. Mahowald et al. on "Relative importance of climate and land use in determining present and future global soil dust emission", *Geophys. Res. Lett.*, *31*, L24106, doi:10.1029/2004GL021560.
Textor, C., et al. (2005), Analysis and quantification of the diversities of aerosol life cycles within AEROCOM, *Atmos. Chem. Phys. Discuss.*, *5*, 8331–8420.
Torres, O., P. K. Bhartia, J. R. Herman, A. Sinyuk, P. Ginoux, and B. Holben (2002), A long-term record of aerosol optical depth from TOMS observations and comparison to AERONET measurements, *J. Atmos. Sci.*, *59*, 398–413.
VanCuren, R. A., and T. A. Cahill (2002), Asian aerosols in North America: Frequency and concentration of fine dust, *J. Geophys. Res.*, *107*(D24), 4804, doi:10.1029/2002JD002204.
Volz, F. E. (1973), Infrared optical constants of ammonium sulfate, Sahara dust, volcanic pumice and flyash, *Appl. Opt.*, *12*, 564–568.
Wesely, M. L., and B. B. Hicks (1977), Some factors that affect the deposition rates of sulfur dioxide and similar gases on vegetation, *J. Air Pollut. Control Assoc.*, *27*, 1110–1116.
Xie, P., and A. Arkin (1997), Global precipitation: A 17-year monthly analysis based on gauge observations, satellite estimates, and numerical model outputs, *Bull. Am. Meteorol. Soc.*, *78*, 2539–2558.
Zender, C. S., D. Newman, and O. Torres (2003), Spatial heterogeneity in aeolian erodibility: Uniform, topographic, geomorphic, and hydrologic hypotheses, *J. Geophys. Res.*, *108*(D17), 4543, doi:10.1029/2002JD003039.
Zender, C. S., R. L. Miller, and I. Tegen (2004), Quantifying mineral dust mass budgets: Systematic terminology, constraints, and current estimates, *Eos Trans. AGU*, *85*(48), 509, 512.
Zhou, Z. J., and G. C. Zhang (2003), Typical severe dust storms in northern China during 1954–2002, *Chin. Sci. Bull.*, *48*, 2366–2370.
Zobler, L. (1986), A world file for global climate modeling, *NASA Tech. Rep., TM-87802*, 32 pp.

R. V. Cakmur, I. Geogdzhayev, D. Koch, R. Ruedy, and G. A. Schmidt, NASA Goddard Institute for Space Studies, 2880 Broadway, New York, NY 10025, USA. (rcakmur@giss.nasa.gov; igeogdzhayev@giss.nasa.gov; dkoch@giss.nasa. gov; rruedy@giss.nasa.gov; gschmidt@giss.nasa.gov)

P. Ginoux, Geophysical Fluid Dynamics Laboratory, NOAA, Princeton Forrestal Campus Route 1, P.O. Box 308, Princeton, NJ 08542-0308, USA. (paul.ginoux@noaa.gov)

K. E. Kohfeld, School of Earth and Environmental Sciences, Queens College, City University of New York, 65-30 Kissena Blvd., Flushing, NY 11367, USA. (kek@qc.edu)

R. L. Miller and J. Perlwitz, Department of Applied Physics and Applied Math, Columbia University, 2880 Broadway, New York, NY 10025, USA. (rlm15@columbia.edu; jp544@columbia.edu)

C. Prigent, Laboratoire d'Études du Rayonnement et de la Matière en Astrophysique, Observatoire de Paris, CNRS, 61, Avenue de l'Observatoire, F-75014 Paris, France. (catherine.prigent@obspm.fr)

I. Tegen, Leibniz Institute for Tropospheric Research, Permoserstr. 15, 04318 Leipzig, Germany. (itegen@tropos.de)